

Hybrid RANS/LES simulations of the turbulent flow over periodic hills at high Reynolds number using the PITM method

Bruno Chaouat*

ONERA , 92322 Châtillon, France

Roland Schiestel**

IRPHE, Château-Gombert, 13384 Marseille, France

Abstract

We apply the partially integrated transport modeling (PITM) method with a stress transport subfilter model [Chaouat, B. and Schiestel, R., “A new partially integrated transport model for subgrid-scale stresses and dissipation rate for turbulent developing flows”, *Physics of Fluids*, Vol. 17., 2005] to perform continuous hybrid non-zonal RANS/LES numerical simulations of turbulent flows over two-dimensional periodic hills at high Reynolds number $Re = 37000$ on coarse and medium meshes. The fine scale turbulence is described using a subfilter scale stress transport model deduced from PITM. This work extends the previous simulations of the turbulent flow over periodic hills performed at the lower Reynolds number $Re = 10595$ [Chaouat, B., “Subfilter-scale transport model for hybrid RANS/LES simulations applied to a complex bounded flow”, *Journal of Turbulence*, Vol. 11, 2010] to the higher value 37000 considering that studying the effects of the Reynolds number on the turbulence field constitutes a new material that deserves interest in CFD. So that, the aim of this paper is to explore the extension of a PITM subfilter model to high Reynolds numbers where conventional LES is not any more accessible because of the highly consuming cost. The effects of the grid refinement at $Re = 37000$ are investigated in detail through the use of different mesh sizes with a very coarse grid and with a several medium grids. For comparison purposes, the channel flow over 2D hills is also computed using a full statistical Reynolds stress transport model developed in RANS methodology. As a result of the simulations, it appears that the PITM simulations, although performed on coarse meshes, reproduce this complex flow governed by interacting turbulence mechanisms associated with separation, recirculation, reattachment, acceleration and wall effects with a relatively good agreement. The mean velocity and turbulent stresses are compared with reference data of this experiment at the flow Reynolds number $Re = 37000$ [Rapp, Ch. and Manhart, M., “Flow over periodic hills - an experimental study”, *Experiments in Fluids*,

*Senior Scientist, Department of Computational Fluid Dynamics.

**Senior Scientist at CNRS.

Vol. 51., 2011]. Some discrepancies are observed in the immediate vicinity of the lower wall for the coarse simulations but as it could be expected, the simulation performed on the medium mesh provides better results than those performed on the coarse meshes thanks to the higher resolution due to the grid refinement in the streamwise and spanwise directions that allows a better account of the three-dimensional character of the flow. As usual in LES calculations, the instantaneous large flow structures are investigated in detail providing some interesting insights into the structures of the present turbulent flow. Comparatively to the PITM simulation results, it is found that the RANS Reynolds stress model based on second moment closures fails to predict correctly this flow in several respects, although being one of the most advanced model in RANS methodology. Important discrepancies with the experimental data are noticed. This work suggests that the present subfilter-scale stress model derived from the PITM method is well suited for simulating complex flows at high Reynolds numbers, with a sufficient accuracy from an engineering point of view, even if the grids are not as so fine as those used in conventional LES, while at the same time allowing a drastic reduction of the computational cost. Beside, these calculations give some ideas on the influence of the Reynolds number on the flow.

1 Introduction

Usually, the Reynolds averaged Navier-Stokes (RANS) methodology based on a statistical averaging (or in practice a long-time averaging which is sufficiently large in comparison with the turbulence time scale [1]) and particularly the route of advanced Reynolds stress transport modeling (RSM) developed in the framework of second-moment closures (SMC)[2, 3], appears as an efficient way for tackling engineering flows encountered in aeronautics applications with reasonable computational costs [4]. However, although reaching a high level of sophistication in RANS methodology, RSM models may show some weaknesses in simulating turbulent flows in which the unsteady large scales play an important role. This happens in particular situations where the mean flow quantities are strongly affected by the dynamic of large scale turbulent eddies [5, 6, 7]. Indeed, RANS models seem working well in flow situations where the time variations in the mean flow are of much lower frequency than the turbulence itself. This is the favored field of application of RANS and unsteady RANS (URANS). On the other hand, highly resolved large-eddy simulation (LES) which consists in modeling the more universal small scales while the large scales motions are explicitly calculated, is a promising route. It is now largely developed [8] when insight in the turbulence structure is required. But, up to now, the LES approach is not affordable for industrial applications involving large computational domains, even with the rapid increase of super-computer power [9]. For instance, an LES simulation of the flow around an entire aircraft still remains out of scope at present time. This problem is particularly acute at high Reynolds numbers since the Kolmogorov scale decreases according to the $R_t^{-9/4}$ law. For these reasons related to high computational costs, new turbulence approaches that combine the advantages of both RANS and LES methods have been recently proposed to simulate engineering or industrial flows. They are essentially based on hybrid zonal methods for which a thorough review conducted by Fröhlich *et al.* can be found in reference [10]. Among these hybrid RANS/LES methods, the detached eddy simulation (DES) developed by Spalart and co-authors [9, 11], or in an improved version, the delayed DES [12], where the model

is switching from a RANS behavior to an LES behavior, depending on a criterion based on the turbulent length scale, is certainly one of the most popular models. As a practical method for handling aeronautical applications, DES is often used to simulate flows around obstacles with the aim to access global coefficients such as the drag, lift and pressure coefficients which are useful in the aerodynamic design optimization of aircraft wings. One can also mention the scale-adaptive simulation (SAS) model developed recently [13]. Still from a practical point of view, the DES technique was recently applied to derive the zonal SST-DES model [14] inspired from the SST model developed by Menter [15]. This model has been used for simulating flows around a complete aircraft without and with engine nacelle. Some other RANS/LES zonal methods have also been developed in this spirit but they rely on two different models, a RANS model and a subgrid-scale model, which are applied in different domains separated by an artificial interface [16, 17, 18]. Although zonal hybrid RANS/LES models are of practical use in a general way, allowing a reduction of the computational cost compared to conventional LES, the RANS/LES interface still poses matching problems between the RANS and LES regions. The interface is empirically located inside the computational domain and the turbulence closure suddenly changes from one region to another adjacent one without continuity when crossing the interface. Furthermore, these methods often require an internal forcing produced by artificial instantaneous random fluctuations for restoring continuity of turbulence levels at the crossflow between these domains. Extra terms introduced in the equations are then necessary to get the correct velocity and stress profiles in the boundary layer [10, 19]. The question of the log-layer mismatch velocity for hybrid RANS/LES simulations has been addressed in detail by Hamba in reference [20].

In the field of hybrid RANS-LES methods, Schiestel and Dejoan [5], and Chaouat and Schiestel [6, 21] have developed the partially integrated transport modeling (PITM) method with seamless coupling changing smoothly from RANS to LES in different regions in order to overcome the difficulties raised by zonal models mentioned above. From this method, these authors have derived subfilter turbulence models, the former one using an energy transport model with a subfilter viscosity and the latter one using a stress transport model based on second-moment closure (SMC). From a physical standpoint, this method has been derived in the spectral space by considering the Fourier transform of the dynamic equation for the two-point velocity fluctuating correlations [22]. Then, partial integration of these spectral equation gives rise to subfilter turbulence models including a new transport equation for the dissipation rate which constitutes the main ingredient of the PITM method. Contrarily to zonal hybrid RANS/LES models, the subfilter models derived from the PITM method vary continuously from RANS to LES with respect to a parameter formed from the ratio of the turbulent length-scale to the grid-size L_e/Δ so that there are no discrete interfaces between the RANS and LES regions. Almost any usual statistical RANS model can be transposed into its subfilter version, using the PITM method. In turbulence modeling, subfilter scale stress transport models developed in the framework of SMC [6, 7, 23, 24] are probably among the most elaborated models transposed from RSM models [25, 26]. Indeed, the use of transport equations for the subfilter-scale stress components allows to take into account more precisely the turbulent processes of production, transfer, pressure redistribution effects and dissipation, in a better way than eddy viscosity models. Due to the presence of the material derivative in the stress transport equations, the subfilter-scale stress model is able to account for some history effects in

the turbulence interactions, and also due to the presence of pressure-strain correlation terms, to describe more faithfully the anisotropy of the turbulence field. Moreover, some backscatter effects can possibly arise because the production term in the stress equations can indeed become negative in some places, contrarily to what happens in two equation closures based on eddy viscosity in which the production term is strictly positive. Consequently, subfilter stress models offer various interesting potentialities for simulating non-equilibrium unsteady flows. Subfilter-scale stress models are however more often used in research codes rather than in industrial numerical simulation codes, the reason being that viscosity models accounting for two transport equations are obviously easier to implement and to run in CFD codes than Reynolds stress models accounting for seven strongly coupled equations in unsteady flow evolution. [27]. Moreover, second moment turbulence closure may pose some numerical difficulties. Indeed, in two equation eddy viscosity models, the turbulence stresses are usually treated numerically as diffusion terms that have a stabilizing effect in the momentum equation, whereas in second moment closures, the stresses are numerically integrated as external source terms that have in the contrary a destabilizing effect on the motion equation. We will see in the following what stabilization techniques have been used for overcoming these difficulties. The PITM concept for the dissipation rate equation is also particularly appealing for turbulent flows with some departures from the standard Kolmogorov equilibrium law while using relatively coarse grids [21, 23]. Furthermore, these models can also be used in the perspective to investigate turbulent flows with emphasis on fundamental aspect and structural aspects, together with statistical post-analysis based on two-point correlations and spectral properties. Of course, it is not expected to get the accuracy of conventional fine grid LES in the structural description, but some useful trends are however possible, as exemplified further, the aim being to get acceptable results while reducing the computational cost. Another approach is the PANS (partially averaged Navier-Stokes) method [28] based on the self-similarity scale assumption which in fact leads to transport equations that look very similar to the ones obtained from the PITM method but they have been developed in a totally different line of thought and different arguments. Moreover, the PANS model does not provide a defined link between the model equations and the filter size since the ratio of the subfilter-energy to the total energy is arbitrarily prescribed. The results are then depending on this prescribed ratio and the role of the filter is disconnected and cannot be clearly interpreted from a physical point of view. This is not satisfactory on the physical point of view, as it was discussed in detail in reference [29].

This paper first briefly recalls the main principles of the partially integrated transport modeling method developed in the spectral space. Then hybrid RANS/LES numerical simulations of the turbulent flow over periodic hills are performed on coarse and medium meshes at a high Reynolds number $Re = 37000$. This test case of a channel with streamwise periodic constrictions and separation is of practical interest in the field of aerodynamic applications because of the presence and interaction of turbulence mechanisms associated with separation, recirculation, reattachment, acceleration and wall vicinity effects that are often encountered in industrial and aerospace flows. A special attention is therefore devoted to these mechanisms occurring in the flow at the high Reynolds number $Re = 37000$ comparatively to those previously studied at a lower Reynolds number $Re = 10595$ [7, 30, 31]. For comparison purposes, RANS computations of the same channel flow over 2D hills using a statistical Reynolds stress model are also performed on the coarse mesh, also at the same Reynolds number $Re = 37000$. For each simulation, the mean velocity and turbulent

stresses components returned by the PITM simulation and the RSM prediction are compared with the experimental data at $Re = 37000$ obtained by Rapp [32, 33]. The conditions of realizability of the turbulent stresses are checked from a few solution trajectories projected onto the plane formed by the second and third invariants in the diagram of Lumley [34]. This also allows to assess the turbulence model in its capability to reproduce correctly the flow anisotropy by determining the possible turbulence states in this diagram. With the aim to investigate the flow from a spectral point of view, energy spectrum densities are performed using the Fourier transform of the instantaneous velocities. The two-point fluctuating velocity correlations are computed in the spanwise direction of the channel to get statistical information. Moreover, interest is then placed on some structural aspects of this complex flow.

2 The filtering and averaging processes

Turbulent flows of a viscous incompressible fluid are considered. In large eddy simulations, any flow variable ϕ is decomposed into a large scale (or resolved) part $\bar{\phi}$ and a subfilter fine scale (or modeled) part $\phi^>$. Both are fluctuating. The large scale component is defined by the filter function G_Δ as

$$\bar{\phi}(\mathbf{x}) = \iiint_{\mathcal{D}} G_\Delta(\mathbf{x} - \mathbf{y}) \phi(\mathbf{y}) d^3\mathbf{y} \quad (1)$$

where Δ denotes the filter width. In view of the statistical averaging process, the instantaneous variable ϕ can also be decomposed into a statistical mean part $\langle\phi\rangle$ and a fluctuating part ϕ' leading to $\phi = \langle\phi\rangle + \phi'$. The instantaneous fluctuation ϕ' contains in fact the large scale fluctuating part $\phi^<$ and the small scale fluctuating part $\phi^>$ such that $\phi' = \phi^< + \phi^>$. So that ϕ can then be rewritten as the sum of a mean statistical part $\langle\phi\rangle$, a large scale fluctuating part $\phi^<$ and a small scale fluctuating part $\phi^>$ as follows $\phi = \langle\phi\rangle + \phi^< + \phi^>$. The first two terms correspond to the filtered velocity $\bar{\phi} = \langle\phi\rangle + \phi^<$ implying that the large scale fluctuating part is simply the difference between the filtered and the statistical quantities, $\phi^< = \bar{\phi} - \langle\phi\rangle$. In fact, the large scale fluctuations (resolved scales) and the fine scales fluctuations (modeled scales) can be naturally defined from the physical meaning of the Fourier transform of the fluctuating quantities ϕ' using the cutoff wavenumber κ_c as the lower bound of the integration interval. Indeed, if working in spectral space, the large scale $\phi^<$ and the fine scale $\phi^>$ are then defined from the Fourier transforms as [22]

$$\phi^<(\mathbf{x}) = \int_{|\kappa| \leq \kappa_c} \hat{\phi}'(\boldsymbol{\kappa}) \exp(j\boldsymbol{\kappa}\mathbf{x}) d\boldsymbol{\kappa} \quad (2)$$

$$\phi^>(\mathbf{x}) = \int_{|\kappa| \geq \kappa_c} \hat{\phi}'(\boldsymbol{\kappa}) \exp(j\boldsymbol{\kappa}\mathbf{x}) d\boldsymbol{\kappa} \quad (3)$$

where the Fourier transform $\hat{\phi}'(\boldsymbol{\kappa})$ is defined as usually from

$$\hat{\phi}'(\boldsymbol{\kappa}) = \frac{1}{(2\pi)^3} \int_{R^3} \phi(\mathbf{x}) \exp(-j\boldsymbol{\kappa}\mathbf{x}) d\mathbf{x} \quad (4)$$

Note that all the previous relations are exact only in homogeneous turbulence and only approximate in locally homogeneous turbulence [22]. Applying the filtering operation to the instantaneous

Navier-Stokes momentum equation yields the filtered equation

$$\frac{\partial \bar{u}_i}{\partial t} + \frac{\partial}{\partial x_j} (\bar{u}_i \bar{u}_j) = -\frac{1}{\rho} \frac{\partial \bar{p}}{\partial x_i} + \nu \frac{\partial^2 \bar{u}_i}{\partial x_j \partial x_j} - \frac{\partial (\tau_{ij})_{sfs}}{\partial x_j} \quad (5)$$

where u_i , p , ν , $(\tau_{ij})_{sfs}$, are the velocity vector, the pressure, the molecular viscosity and the subfilter-scale stress tensor, respectively. The subfilter-scale tensor $(\tau_{ij})_{sfs}$ is defined by the mathematical relation

$$(\tau_{ij})_{sfs} = \overline{u_i u_j} - \bar{u}_i \bar{u}_j \quad (6)$$

The presence of the turbulent contribution $(\tau_{ij})_{sfs}$ in equation (5) indicates the effect of the subfilter scales on the resolved field. The resolved scale tensor is defined by the relation

$$(\tau_{ij})_{les} = \bar{u}_i \bar{u}_j - \langle u_i \rangle \langle u_j \rangle \quad (7)$$

It can be shown that for spectral cutoff filters defined from the Fourier transform [35, 36], the large scale and small scale fluctuations are uncorrelated and the full Reynolds stress tensor τ_{ij} including the small and large scale fluctuating velocities can be computed as the sum of the subfilter and the resolved stress tensors

$$\tau_{ij} = \langle (\tau_{ij})_{sfs} \rangle + \langle (\tau_{ij})_{les} \rangle \quad (8)$$

whereas the statistical turbulent kinetic energy is obtained as the half-trace of the stress tensor τ_{ij} leading to

$$k = \langle k_{sfs} \rangle + \langle k_{les} \rangle \quad (9)$$

The relationships (2) and (3) are strictly valid for homogeneous turbulence and still remain however a good approximation in the case of non-homogeneous turbulence. As usually made in LES simulations, the statistical average of the resolved stresses $\langle (\tau_{ij})_{les} \rangle$ which corresponds to the velocity correlation in the large scale fluctuations $\langle u_i^< u_j^<$ appearing in equation (8) is computed by a numerical procedure using the relation

$$\langle (\tau_{ij})_{les} \rangle = \langle u_i^< u_j^< \rangle = \langle \bar{u}_i \bar{u}_j \rangle - \langle \bar{u}_i \rangle \langle \bar{u}_j \rangle \quad (10)$$

3 Application of the PITM method

3.1 General formalism

The PITM method finds its basic foundation in the spectral space by considering the Fourier transform of the two-point fluctuating velocity correlation equations in homogeneous turbulence [5, 22], the extension to non-homogeneous turbulence being developed within the framework of the tangent homogeneous space [22, 37]. Along the same guidelines, a formalism based on a temporal filtering has been also proposed recently to handle non-homogeneous flows leading to a variant of the PITM method using temporal filters and called temporal partial integrated transport modeling (TPITM) method [24]. The resulting equations are similar in practice. The PITM method is general and allows to derive subfilter scale models with the aim to perform continuous hybrid

non-zonal RANS/LES simulations regardless of the filter width. This is particularly interesting for relatively coarse grids (as far as the grid size is sufficient to describe correctly the mean flow!). These derived subfilter models include both energy transport models using a subfilter eddy viscosity coefficient [5, 38, 39] and stress transport models [6, 7, 23, 24], depending on the chosen level of closure. In the present case, a Reynolds stress transport model inspired from the Launder and Shima well known model [25] has been considered and then turned into a subfilter scale stress transport model. It is based on the transport equations for the subfilter-scale stresses $(\tau_{ij})_{sfs}$ and the subfilter transfer rate ϵ_{sfs} and constitutes therefore in its formulation one of the most elaborated model used in LES methodology [23]. As a result, it formally looks like the corresponding RANS/RSM model but the coefficients used in the model are no longer constants. They are now some functions of the dimensionless cutoff parameter $\eta_c = \kappa_c L_e$ involving the cutoff wave number $\kappa_c = \pi/\Delta$ and the integral turbulent length scale $L_e = k^{3/2}/\epsilon$ built using the total turbulent kinetic energy $k = \langle k_{sfs} \rangle + \langle k_{les} \rangle$, the total dissipation rate $\epsilon = \langle \epsilon_{sfs} \rangle + \langle \epsilon^< \rangle$, itself composed of the subfilter transfer rate ϵ_{sfs} and the resolved large scale dissipation rate $\epsilon^<$ which becomes not negligible in low Reynolds number flows. In order to account in a simple way for the anisotropy of the grid near the walls, the effective filter Δ is defined by [40]

$$\Delta = \zeta \Delta_a + (1 - \zeta) \Delta_b \quad (11)$$

where the filters lengths Δ_a and Δ_b are defined by $\Delta_a = (\Delta_1 \Delta_2 \Delta_3)^{1/3}$ and $\Delta_b = [(\Delta_1^2 + \Delta_2^2 + \Delta_3^2)/3]^{1/2}$ and where ζ is a parameter set to 0.8.

3.2 Subfilter scale stress transport equation

By using the material derivative operator in the filtered field $D/Dt = \partial/\partial t + \bar{u}_k \partial/\partial x_k$, the transport equation for the subfilter stress tensor can be written in the simple compact form as

$$\frac{D(\tau_{ij})_{sfs}}{Dt} = P_{ij} + \Pi_{ij} + J_{ij} - (\epsilon_{ij})_{sfs} \quad (12)$$

where the terms appearing in the right-hand side of this equation are identified as production, redistribution, diffusion and dissipation, respectively. The transport equation for the subfilter turbulent energy is obtained as half the trace of equation (12)

$$\frac{D(k_{sfs})}{Dt} = P + J - \epsilon_{sfs} \quad (13)$$

where $P = P_{mm}/2$, $J = J_{mm}/2$, $\epsilon_{sfs} = (\epsilon_{mm})_{sfs}/2$. The precise expressions of the terms P_{ij} , Π_{ij} and J_{ij} appearing in equation (12) are recalled in appendix A.

3.3 Subfilter dissipation-rate transport equation

Closure of equation (12) needs to model the subfilter tensorial transfer rate $(\epsilon_{ij})_{sfs}$ which is approached by $2/3 \epsilon_{sfs} \delta_{ij}$. The modeling of the transfer-rate ϵ_{sfs} is made by means of its transport equation which is obtained from the PITM method using spectral splitting techniques and partial integrations. This transfer-rate equation formally looks like the usual dissipation-rate equation

used in statistical models but the coefficients are no longer constants and differ in their numerical values. As a result of the modeling procedure [5, 6], the transport equation for the subfilter transfer-rate reads

$$\frac{D\epsilon_{sfs}}{Dt} = c_{sfs\epsilon_1} \frac{\epsilon_{sfs}}{k_{sfs}} P - c_{sfs\epsilon_2} \frac{\epsilon_{sfs}\tilde{\epsilon}_{sfs}}{k_{sfs}} + J_\epsilon \quad (14)$$

where J_ϵ denotes the diffusion term (see appendix A) and where $\tilde{\epsilon}_{sfs} = \epsilon_{sfs} - 2\nu(\partial\sqrt{k_{sfs}}/\partial x_n)^2$ includes the usual empirical near wall correction used in statistical models and in which x_n denotes the coordinate normal to the wall. In this equation, the coefficient $c_{sfs\epsilon_1}$ appearing in the source term of the transfer-rate equation is the same as the one used in the corresponding RANS dissipation equation $c_{sfs\epsilon_1} = c_{\epsilon_1}$ whereas the coefficient $c_{sfs\epsilon_2}$ appearing in the destruction term of the transfer-rate equation is now given by

$$c_{sfs\epsilon_2} = c_{\epsilon_1} + \frac{\langle k_{sfs} \rangle}{k} (c_{\epsilon_2} - c_{\epsilon_1}) \quad (15)$$

where c_{ϵ_2} is the constant used in the statistical RANS dissipation-rate equation. The ratio $\langle k_{sfs} \rangle / k$ appearing in equation (15) is evaluated by reference to an analytical energy spectrum $E(\kappa)$ inspired from a Von Kármán spectrum considered as a limiting equilibrium distribution. Analytical developments lead to the final result [23]

$$c_{sfs\epsilon_2}(\eta_c) = c_{\epsilon_1} + \frac{c_{\epsilon_2} - c_{\epsilon_1}}{[1 + \beta_\eta \eta_c^3]^{2/9}} \quad (16)$$

Equation (16) indicates that the parameter η_c acts like a dynamic parameter which controls the location of the cutoff within the energy spectrum and the value of the function $c_{sfs\epsilon_2}$ then controls the relative amount of turbulence energy contained in the subfilter range. The theoretical value of the coefficient β_η in equation (16) has been found to be $\beta_{\eta\tau} = [2/(3C_K)]^{9/2}$ [5, 22] where C_K is the Kolmogorov constant.

4 Numerical method

4.1 Numerical schemes

The present numerical simulations are performed using an efficient research code [41] based on a finite volume technique that has been previously tested on several laboratory and aerodynamic laminar and turbulent flows. The software can handle both compressible flows and almost incompressible flows. The equations are integrated in time using an explicit Runge-Kutta scheme of fourth-order accuracy along with an implicit iterative scheme for solving the source terms. The global scheme reads

$$\mathbf{U}^{n+1} = \mathbf{U}^n + \delta t \sum_{k=1}^K \beta_k G(\mathbf{U}^{(k)}) \quad (17)$$

with

$$\mathbf{U}^{(k)} = \mathbf{U}^{(k')} + \alpha_k \delta t S(\mathbf{U}^{(k)}, \mathbf{U}^{(k')}) \quad (18)$$

where

$$\mathbf{U}^{(k')} = \mathbf{U}^n + \alpha_k \delta t G \left(\mathbf{U}^{(k-1)} \right) \quad (19)$$

In these equations, \mathbf{U} is the vector for the mean and turbulent flow variables, G denotes the convective and diffusive flux contributions, S corresponds to the source terms, α_k and β_k are the Runge-Kutta coefficient values given by $\alpha_1 = 0$, $\alpha_2 = \alpha_3 = 1/2$, $\alpha_4 = 1$, $\beta_1 = \beta_4 = 1/6$, $\beta_2 = \beta_3 = 1/3$, and the index (k) denotes the step of the Runge-Kutta method. At the beginning of the procedure, $\mathbf{U}^{(0)} = \mathbf{U}^n$. The numerical method used to solve the instantaneous equations for the subfilter scale turbulent stresses and transfer-rate equations deserves specific attention. Indeed these equations are stiff and they are governed by highly non-linear source terms that evolve rapidly in time and space in comparison with the convective and diffusive terms that present a smoother variation. These equations pose some numerical difficulties in terms of stability and accuracy so that an implicit iterative algorithms in time have been especially developed. The first step in the numerical procedure consists in solving the equation for the subfilter turbulent energy (13) and the equation for the subfilter transfer-rate (14) that are strongly coupled to each other. The equation for the subfilter turbulent energy is indeed mathematically redundant with the stress equations but this practice improves numerical stability. Afterward, in a second step, the individual subfilter turbulent stress equations (12) are then solved using the preceding values found for k_{sfs} and ϵ_{sfs} . Considering the time advancement $\alpha_k \delta t$ of equation (18), the turbulent equations for the subfilter turbulent energy k_{sfs} and the dissipation-rate ϵ_{sfs} are discretized implicitly in time by linearizing the source terms as follows

$$\frac{k_{sfs}^{p+1} - k_{sfs}^{(k')}}{\alpha_k \delta t} = P^p - \omega_{sfs}^p k_{sfs}^{p+1} \quad (20)$$

and

$$\frac{\epsilon_{sfs}^{p+1} - \epsilon_{sfs}^{(k')}}{\alpha_k \delta t} = \omega_{sfs}^p \left(c_{\epsilon_1} P^p - c_{sfs\epsilon_2} \epsilon_{sfs}^{p+1} \right) \quad (21)$$

where $\omega_{sfs} = \epsilon_{sfs}/k_{sfs}$ is the characteristic frequency of the turbulence leading to the solutions

$$k_{sfs}^{p+1} = \frac{k_{sfs}^{(k')} + P^p \alpha_k \delta t}{1 + \omega_{sfs}^p \alpha_k \delta t} \quad (22)$$

and

$$\epsilon_{sfs}^{p+1} = \frac{\epsilon_{sfs}^{(k')} + c_{\epsilon_1} \omega_{sfs}^p P^p \alpha_k \delta t}{1 + c_{sfs\epsilon_2} \omega_{sfs}^p \alpha_k \delta t} \quad (23)$$

where the turbulent variables are initialized by $k_{sfs}^1 = k_{sfs}^{(k')}$ and $\epsilon_{sfs}^1 = \epsilon_{sfs}^{(k')}$ for $p = 1$. The question now is to solve the transport equation (12) of the subfilter turbulent stress by an efficient iterative algorithm. To do that, one can remark that this equation can be formally rewritten into a linearized expression including only two different contributions in a such a way that the temporal term $\partial(\tau_{ij})_{sfs}/\partial t$ becomes a function of the stress $(\tau_{ij})_{sfs}$ appearing in the right-hand side of this equation as follows

$$\frac{\partial(\tau_{ij})_{sfs}}{\partial t} = F_{ij} - c_1 \omega_{sfs} (\tau_{ij})_{sfs} \quad (24)$$

where F_{ij} denotes the tensorial function of the subfilter stress, dissipation rate and main velocity gradient (see appendix A) that reads

$$F_{ij} = P_{ij} - c_2 \left(P_{ij} - \frac{2}{3} P \delta_{ij} \right) + \frac{2}{3} c_1 \omega_{sfs} k_{sfs} \delta_{ij} - \frac{2}{3} \epsilon_{sfs} \delta_{ij} \quad (25)$$

and where P_{ij} is the production term caused by the interaction between the stresses and the velocity gradients

$$P_{ij} = -(\tau_{ik})_{sfs} \frac{\partial \bar{u}_j}{\partial x_k} - (\tau_{jk})_{sfs} \frac{\partial \bar{u}_i}{\partial x_k} \quad (26)$$

In equation (25), c_1 and c_2 are some functions of the invariant tensors defined in appendix A. Equations (25) and (26) show clearly that $F_{ij} = F_{ij}[k_{sfs}, \epsilon_{sfs}, (\tau_{ik})_{sfs}, (\tau_{jk})_{sfs}]$. Equation (24) is then discretized under an implicit form with respect to the subfilter stress $(\tau_{ij})_{sfs}$ taking into account the preceding values k_{sfs}^{p+1} and ϵ_{sfs}^{p+1} already computed by equations (22) and (23) as follows

$$\frac{(\tau_{ij})_{sfs}^{p+1} - (\tau_{ij})_{sfs}^{(k')}}{\alpha_k \delta t} = F_{ij}[k_{sfs}^{p+1}, \epsilon_{sfs}^{p+1}, (\tau_{ik})_{sfs}^p, (\tau_{jk})_{sfs}^p] - c_1 \omega_{sfs}^{p+1} (\tau_{ij})_{sfs}^{p+1} \quad (27)$$

leading to the solution $(\tau_{ij})_{sfs}^{p+1}$ that finally reads

$$(\tau_{ij})_{sfs}^{p+1} = \frac{(\tau_{ij})_{sfs}^{(k')} + F_{ij}[k_{sfs}^{p+1}, \epsilon_{sfs}^{p+1}, (\tau_{ik})_{sfs}^p, (\tau_{jk})_{sfs}^p] \alpha_k \delta t}{1 + c_1 \omega_{sfs}^{p+1} \alpha_k \delta t} \quad (28)$$

or equivalently

$$(\tau_{ij})_{sfs}^{p+1} = \frac{(\tau_{ij})_{sfs}^{(k')} + [P_{ij}^p - c_2 \left(P_{ij}^p - \frac{2}{3} P^p \delta_{ij} \right) + \frac{2}{3} (c_1 - 1) \epsilon_{sfs}^{p+1} \delta_{ij}] \alpha_k \delta t}{1 + c_1 \omega_{sfs}^{p+1} \alpha_k \delta t} \quad (29)$$

where the subfilter stress is initialized by $(\tau_{ij})_{sfs}^1 = (\tau_{ij})_{sfs}^{(k')}$ for $p = 1$. The converged solutions of the iterative algorithms are obtained when $k_{sfs}^{(k)} = \lim_{p \rightarrow \infty} k_{sfs}^p$, $\epsilon_{sfs}^{(k)} = \lim_{p \rightarrow \infty} \epsilon_{sfs}^p$ and $(\tau_{ij})_{sfs}^{(k)} = \lim_{p \rightarrow \infty} (\tau_{ij})_{sfs}^p$. It has been checked that the numerical procedure allows to satisfy the trace equality $k_{sfs}^{(k)} = (\tau_{mm})_{sfs}^{(k)}/2$ which is practically verified within two or three internal iterations in practice. Written in these forms, the iterative algorithms (22), (23) and (29) remain stable because of their denominators that are always greater than unity whatever the k_{sfs} and ϵ_{sfs} values. This numerical procedure is repeated at each step ($k=1$ to 4) of the Runge-Kutta method. The numerical algorithms also present the advantage to ensure the positivity of the normal stresses and is able to satisfy the weak form of the realizability constraints [42] in the mathematical sense given by the condition [27]

$$c_1 \geq 1 - c_2 \frac{P}{\epsilon_{sfs}} \quad (30)$$

In practice, the inequality (30) is verified for usual cases of turbulent flows. Note however that in the framework of SMC, and contrarily to first order models using the Boussinesq hypothesis,

the positivity of the production term is not always guaranteed in all circumstances because some backscatter effects are still possible. Regarding the discretization method in space, the numerical scheme is based on a quasi-centered discretized formulation of the mean flow variables. It has a fourth-order accuracy in space capable to accurately simulate the large scales of the flow. Using equations (22), (23) and (29), it has been checked that the scheme remains of fourth-order accuracy in time without introducing additional numerical dissipation. Another point to mention is a convergence enhancement procedure that proved to be useful in practice. The aim of this procedure is to avoid the model to reach a purely RANS or a purely LES limiting behavior during the transitional initial phase of the calculation and also to accelerate the numerical convergence towards the solution in the permanent state. This procedure [21, 43] consists in locally modifying the coefficient $c_{sf s \epsilon_2}$ in order to force the model to approach more rapidly the expected energy ratio, it has been activated during the computations presented here. This procedure finds its physical meaning in reference [29]. This does not alter the accuracy of the instantaneous solution.

4.2 CPU time requirements

The question of CPU time requirements is essential when performing LES simulations. As mentioned by Spalart [9], conventional LES simulation is limited in Reynolds number and still remains out of scope at present time for high Reynolds number. This is one of the practical reasons that has initially motivated the development of the PITM method. In the present case, the subfilter stress model derived from the PITM method needs to solve seven equations for the vector components

$$\mathbf{U} = [(\tau_{11})_{sfs}, (\tau_{12})_{sfs}, (\tau_{13})_{sfs}, (\tau_{22})_{sfs}, (\tau_{23})_{sfs}, (\tau_{33})_{sfs}, \epsilon_{sfs}]^T, \quad (31)$$

in addition to the Navier-Stokes equations. In practice, it has been found that the additional cost requires roughly 30 % to 50 % more CPU time than conventional LES simulations using eddy viscosity models such as, for instance, the dynamic Smagorinsky model (DSM) [44]. This additional time is not really excessive. This is due to the fact that all the stress equations share the same mathematical structure whatever the component $(\tau_{ij})_{sfs}$. All these equations can be written in the same form including convection, diffusion and source terms. So that the system solution can be efficiently optimized using vectorization and parallelization techniques [27]. In the past, several flows encountered in engineering applications have been simulated using subfilter stress models and DSM models. These flow simulations were performed on different grids and the computational times required for these simulations were compared [6, 7, 21]. As a result, it had been found that the higher cost necessary for solving the seven equation system was in fact greatly compensated by the possibility of coarsening the mesh because of a better modeling. More precisely, the number of grid-points can be reduced by a factor 5 to 10 but the additional cost is only multiplied by a factor 1.5 so that the saving time is roughly 60-80 %. The details of these engineering simulations are summarized in table IV of reference [21].

5 Computational framework

5.1 Previous simulations on the flows over periodic hills

In the geometry under consideration, the hills constrict the channel by about one third of its total height and they are spaced at a distance of about 9 hill heights as shown in figure 1. The exact dimensions of the computational domain are $D_1 = 9h$, $D_2 = 4.5h$ and $D_3 = 3.036h$, where h denotes the hill height, respectively in the streamwise, spanwise and normal directions. The flow is naturally unsteady and is governed by the separation in wall boundary layer and three dimensional wall effects. Initially, the flow over periodic hills at the Reynolds number $Re = U_b h / \nu = 10595$ based on the hill height h and the bulk velocity U_b about the hill crest was proposed as a benchmark case at the 10th joint “ERCOFTAC/IAHR/COST Workshop on Refined Turbulence Modeling” [45] for assessing the turbulence models ranging from RANS to LES. This benchmark has confirmed that RANS models performed badly for this flow. Breuer *et al.* [31] performed direct numerical simulations of this flow at $Re = 700, 1400, 2800$ and 5600 on several meshes ranging from $13.1 \cdot 10^6$ to $231 \cdot 10^6$ grid-points using both Cartesian and curvilinear codes. Breuer *et al.* [31] as well as Fröhlich *et al.* [30] then performed highly resolved LES on a refined grid of $5 \cdot 10^6$ and $13.1 \cdot 10^6$ grid points, respectively, using the dynamic Smagorinsky model (DSM) [44] and the wall-adapted local eddy-viscosity (WALE) model [46] at $Re = 10595$. They provided some interesting features of this turbulent flows and a useful reference data base. In the framework of turbulence modeling, Jakirlic *et al.* [47] and Chaouat [7] more recently performed continuous non-zonal hybrid RANS/LES simulations of this flow at $Re=10595$ on relatively coarse meshes of $2.5 \cdot 10^5$ and 10^6 grid points using subfilter transport models derived from the PITM method. Although the coarse resolutions of the grids used in the calculations, they all obtained promising results. In particular, the mean flow variables, including the velocity, the shear stress and the turbulent energy were successfully recovered and the flow structures were also qualitatively well reproduced by the subfilter-scale stress model [7]. The flow over periodic hills at the higher Reynolds number $Re = 37000$ has been investigated by experiment carried out by Rapp and Manhart [32, 33] in a water channel using particle image velocimetry and laser-Doppler anemometry. These authors have measured the mean velocity and turbulent stresses in different sections of the channel. As a result of interest, these authors found that the reattachment length decreases with increasing the Reynolds number and that the streamwise velocity develops an overshoot directly above the hill crest also with increasing the Reynolds number. They observed that the mean streamwise velocity profiles become flatter at a higher Reynolds number as shown in figures 24, 25, 26 and 27 from reference [33]. This effect is particularly pronounced close to the reattachment point $x/h = 4$. Moreover, they found a reduction of the Reynolds stresses level as the flow Reynolds number increases from $Re=10600$ to 37000 as shown in figures 29, 30, 33 and 34 of the reference [33]. Manhart *et al.* [48] have performed numerical simulations of this flow at $Re = 37000$ on several meshes ranging from $1.0 \cdot 10^6$ to $4 \cdot 10^6$ grid-points, using both Cartesian and curvilinear codes, incorporating different turbulent models such as the Smagorinsky model [49], the WALE model [46], the Lagrangian dynamic model [50], the wavelet-based eddy-viscosity subgrid-scale model [51] and the model of Schumann based on one transport equation for the subgrid energy [52]. In their paper, these authors have plotted the mean velocity and shear stress profiles at a few stations in the channel. Although the flow was not thoroughly investigated in all stations where experimental data [32, 33] are available, they

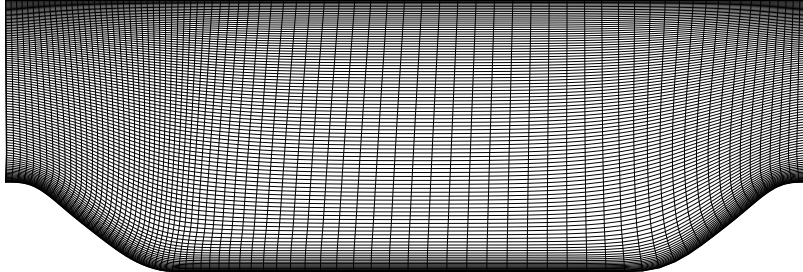


Figure 1: Cross-section of the curvilinear grid 80×100 of the contracted channel.

mentioned certain key features of their simulations in order to get a real comparative insight into these model capabilities. At the Reynolds number $Re = 37000$, these simulations performed on the refined Cartesian mesh of $4 \cdot 10^6$ grid-points using both the WALE and the Lagrangian models (see figure 4 reference [48]) provided satisfactory velocity profiles at the stations $x_1/h = 0.05$ and 4.0 but the results obtained for the medium grid of $2 \cdot 10^6$ grid-points were however disappointing because of the discrepancies observed with the reference data. Furthermore, these authors mentioned in their paper that the Reynolds number dependence of the shear stress was hardly predicted by all the LES simulations under consideration although the Lagrangian and the WALE models provided however better results than the other ones. As expected, the Smagorinsky simulations were unable to satisfactorily predict this flow, even if performed on the refined mesh including some $4 \cdot 10^6$ grid-points. This outcome is not really surprising since the flow over periodic hills is out of spectral equilibrium. That said, the present work will then focus on this higher Reynolds number case $Re = 37000$ giving rise to new comparisons of the PITM simulations with the available experimental data [32, 33].

5.2 Computational resources for DNS or highly resolved LES

As a direct numerical simulation of the flows over periodic hills was already undertaken at the Reynolds number $Re = U_b h / \nu = 5600$ [31], it is worth evaluating, as a rough guide, the necessary computer resources for the Reynolds number $Re = 37000$ in terms of number of necessary grid-points and computational times. A DNS simulation requires that the grid-size is at least of order of magnitude of the Kolmogorov scale η computed as $\eta = (\nu^3 / \epsilon)^{1/4}$. The computational time is proportional to the number of grid points N_η , the number of temporal iterations N_{it} and the time required by the central processing unit t_{CPU} per iteration and per grid-point, leading to the result $t = N_\eta N_{it} t_{CPU}$. In this formula, the number of grid-points N_η is given by

$$N_\eta = \frac{64 D_1 D_2 D_3}{\eta^3} \quad (32)$$

in order to describe a “minimal” sine curve on a full period using at least four grid points. The number of iteration is given by $N_{it} = T / \tau$ where T is the convective time allowing the eddies to move

towards the exit of the channel, whereas τ is the Kolmogorov time scale given by $\tau = \sqrt{\nu/\epsilon} = \eta^2/\nu$. The convective time is computed from $T = D_1/U_b$ where D_1 denotes the dimension of the channel in the streamwise direction so that the computational time is therefore given by

$$t = \frac{64 D_1 D_2 D_3}{\eta^3} \frac{D_1}{U_b} \frac{\nu}{\eta^2} t_{CPU} \quad (33)$$

Although giving a somehow complex expression, equation (33) can be easily simplified if one considers that the turbulent Reynolds number $R_t = L_e \sqrt{k}/\nu = (L_e/\eta)^{4/3}$ is proportional to the mean flow Reynolds number $Re = U_b h/\nu$ in a restricted range of values. Setting $R_t = \zeta Re$, where ζ is an empirical coefficient usually close to 1/10 in confined flows (and in usual Reynolds numbers range), and assuming that the size of the energetic big eddies $L_e = k^{3/2}/\epsilon$ is roughly of order of magnitude of the characteristic geometrical size of the flow itself, equations (32) and (33) can be reduced to more tractable expressions. The number of grid-points and the computational time are then given respectively by $N_\eta = 64 R_t^{9/4}$ and $t = 64 \zeta R_t^{11/4} t_{CPU}$, clearly showing their dependence on the turbulence Reynolds number. Thus, for the two Reynolds numbers considered $Re_1 = 5600$ and $Re_2 = 37000$, one can find that the ratio of the numbers of grid points is $N_{\eta_2}/N_{\eta_1} \approx 70$ ($N_{\eta_2} = 1600 \cdot 10^6$ grid-points if $N_{\eta_1} = 231 \cdot 10^6$) whereas the ratio of the computational times is $t_2/t_1 \approx 1800$. These numerical order of magnitudes clearly shows that DNS (or even highly resolved LES) imply a huge numerical task and still remains difficult to reach in practice at the present time. Considering this fact, we have chosen to rely comparisons of the present PITM simulations completely on experimental data. We stress again that this PITM method is particularly well suited for performing simulations at higher Reynolds numbers without requiring very refined meshes.

5.3 The present simulation for the flows over periodic hills at $Re = 37000$

The objective is to perform PITM simulations of the flow over periodic hills at $Re = 37000$ on coarse and medium meshes and to compare the present results with the experiment carried out by Rapp [32, 33], essentially for the mean velocity and turbulent stresses. Note that to this day, there is no reference LES data for $Re=37000$ so that PITM results can only be compared with experimental data. In this study, a very coarse mesh is deliberately chosen to highlight the ability of the PITM method to simulate large scales of the flow with a sufficient accuracy for engineering computations. The simulations are also performed on several medium meshes for assessing the effects of the grid refinement and for studying the sharing out of the turbulent energy when the filter width is changed. As usually made, a mean pressure gradient term is included in the momentum equations for balancing the viscous friction at the walls and thus forcing the flow. However this forcing is adjusted in time, at each instant, to reach the desired Reynolds number value. So, globally, the numerical method supposes the flow Reynolds number to be chosen at a given value. The statistics of the fluctuating velocity correlations are achieved both in space in the spanwise homogeneous direction and in time using a relaxation relation.

5.4 Boundary conditions

Different boundary conditions are applied on the limits of the computational domain shown in figure 1. The simulated domain is periodic in the streamwise and spanwise directions. The streamwise periodic condition removes the need to specify the inflow and outflow conditions allowing the assessment of the subfilter stress model without any contamination and potential sources of errors in inlet or outlet. No-slip and impermeability boundary conditions are used at the lower and upper walls. The wall sublayers are fully calculated at low Reynolds number without any empirical law of the wall.

5.5 Computational grids

In a previous investigation conducted by Fröhlich *et al.* [30] for the flow simulated at the lower Reynolds number $Re = 10595$, the dimension in the spanwise direction of the computational domain was set to $D_3 = 4.5h$. In a first attempt, this dimension is also retained for performing the PITM simulations at $Re = 37000$. These simulations used a very coarse curvilinear grid of $80 \times 30 \times 100$ points (PITM1) $\approx 1/4$ million grid points, coarse grids $160 \times 30 \times 100$ (PITM2) and $80 \times 60 \times 100$ points (PITM3) $\approx 1/2$ million grid points, and a medium grid of $160 \times 60 \times 100$ points (PITM4) ≈ 1 million grid points respectively in the streamwise, spanwise and normal directions (x_1, x_2, x_3) . As mentioned earlier, the aim is to appreciably reduce the computational cost while reaching acceptable accuracy for applications by using improved modeling. Figure 1 shows the cross-section of the very coarse grid. The grid has been refined in the lower and upper wall regions for accurately computing the boundary layers whereas it get coarser in the center of the channel. As the region beyond the hill constitutes a key region, the grids in the streamwise direction are more refined beyond the hill crest than in the mid-distance of the channel in order to fairly well reproduce the flow separation caused by the hill geometry, and to properly describe the flow recirculation as well as the reattachment of the boundary layer. Figure 2 displays the dimensionless grid spacings in wall unit $\Delta^+ = \Delta u_\tau / \nu$ in the streamwise, spanwise and normal directions where $u_\tau = \sqrt{\tau_w / \rho}$ denotes the shear stress velocity along the lower wall for the PITM1 simulation performed on the very coarse grid. One can see that the computed dimensionless distances Δ_1^+ and Δ_2^+ vary along the lower wall with respect to the streamwise distance, showing a decrease beyond the first hill crest followed by an increase in the windward slope of the second hill crest. From this figure 2, one can see that these two dimensionless distances in the streamwise and spanwise directions largely exceed the minimal limit recommendations for wall-resolved LES given by Piomelli and Chasnov [53]. The dimensionless distance Δ_3^+ in the normal direction to the lower wall varies between 0 and 4 along the streamwise direction except in the windward region of the hill where it reaches higher values because of the increasing friction velocity. These values appear to high to properly describe the boundary layer but this requirement is not crucial here. The results discussed in the next section will show that the PITM simulations allows to obtain satisfactory results without requiring extremely large memory and computing time resources in comparison with those necessary for performing highly resolved academic LES. The fact is that the loss in resolution has to be compensated by improved modeling features. In the PITM approach, the modeled part of the energy spectrum is far more extended than in conventional LES and more advanced models are necessary, giving a renewal of interest for advanced RANS type formalism.

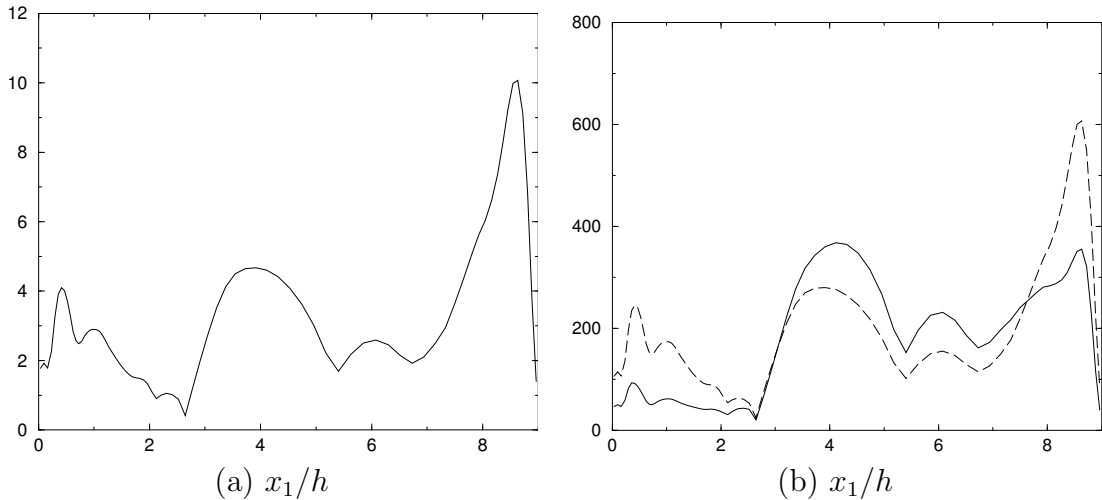


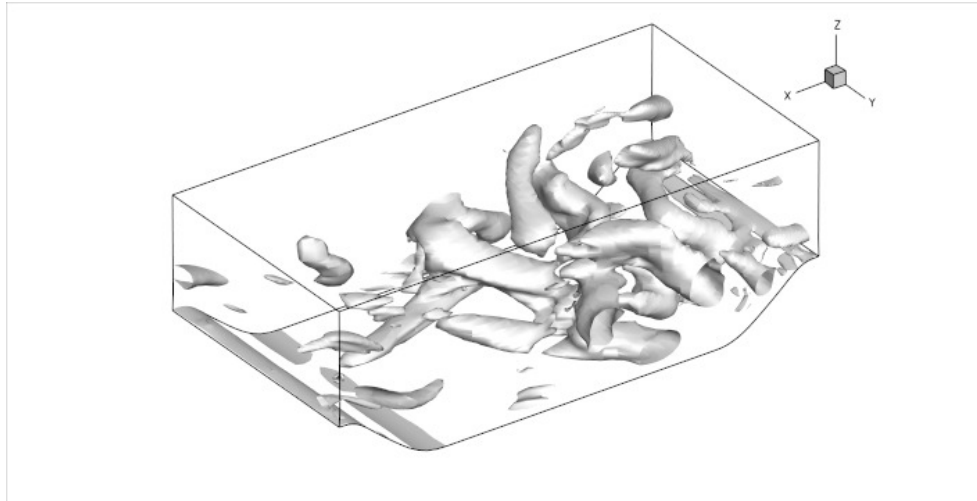
Figure 2. Dimensionless grid spacings in wall units $\Delta^+ = \Delta u_\tau / \nu$ where u_τ is the friction velocity. (a) – normal direction Δ_3^+ ; (b) – streamwise direction Δ_1^+ ; - - spanwise direction Δ_2^+ . PITM1 simulation ($80 \times 30 \times 100$). $Re = 37000$

In the following, the mean flow is obtained by averaging the instantaneous flow in the different planes in the spanwise direction where a periodic condition is applied and in time corresponding to roughly six convective time scale $T = D_1/U_b$ where U_b is the bulk velocity.

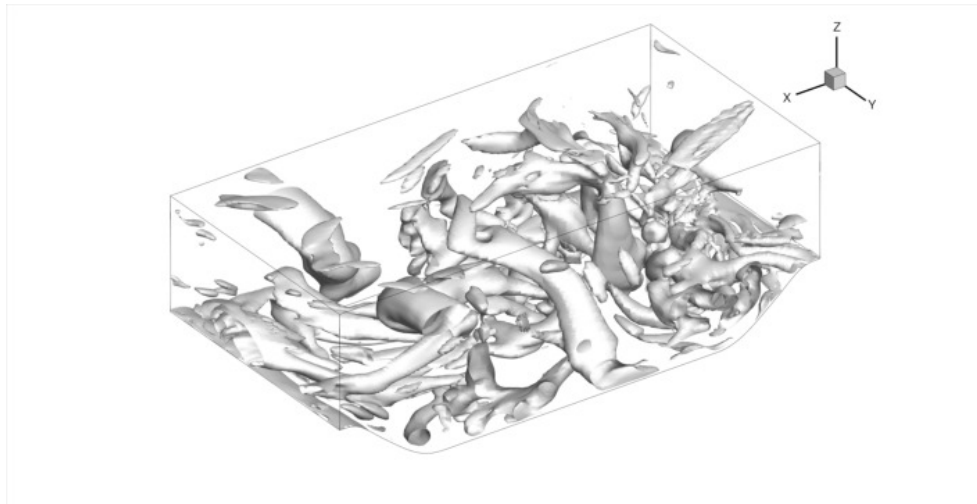
6 Numerical results

6.1 Large flow structures

With the aim to get qualitative insights into the turbulent flow structures that develops inside the channel with periodic hills, large eddies have been depicted using the well known Q criterion [54]. The value of the parameter $Q = \frac{1}{2}(\Omega_{ij}\Omega_{ij} - S_{ij}S_{ij})$ is defined as the balance between the local rotation rate $\mathbf{\Omega}$ and the strain rate \mathbf{S} of the instantaneous velocity, in order to identify packets of flow vortices. As a result, figure 3 (a), (b) shows the Q isosurfaces of the flows performed on the coarse and the medium grids, $80 \times 30 \times 100$ and $160 \times 60 \times 100$, respectively. This figure reveals the presence of very large longitudinal roll cells that develop in the entire channel and clearly demonstrates the three dimensional nature of the flow. Due to the flow recirculation, a strong turbulence activity is visible near the lower wall and particularly concentrated in the leeward region of the second hill. As expected, the PITM4 simulation performed on the medium grid $160 \times 60 \times 100$ captures more resolved scales than the PITM1 simulation leading to the emergence of smaller turbulent roll cells. In that sense, it is clear that a more realistic description of the flow requires a very refined mesh in streamwise, spanwise and normal directions to get the right definition of the structures but as it can be observed from figure 3, it is however remarkable that despite the coarse grid resolution, the PITM simulations still succeeds in qualitatively reproducing



(a)



(b)

Figure 3. Vortical activity illustrated by the Q isosurfaces at $Re = 37000$. (a) PITM1 simulation ($80 \times 30 \times 100$) $Q = 2 \cdot 10^5 s^{-2}$. (b) PITM4 simulation ($160 \times 60 \times 100$) $Q = 4 \cdot 10^5 s^{-2}$.

these dynamic structures. Note that the full statistical RSM computation can only provide mean organized structures and not at all roll cell structures because of the RANS physical foundations. This is true for all RANS models and proper URANS models (which must calculate Reynolds averaged quantities even if unsteady in the mean).

6.2 Streamlines of the flow field

The purpose of this section is to access more practical details of the flow through the study of the streamlines of the flow field with a particular interest focused on the recirculation zone. Figure 4 shows the streamlines plot generated in two dimensions obtained by averaging the PITM velocities both in the homogeneous planes in the spanwise direction and in time as well as the statistical RSM streamlines. The flow separation is caused by the adverse pressure gradient which results from the strong streamwise curvature of the lower wall. For all simulations, the location of the points of separation and reattachment are indicated in Table 1, including also the experimental result given by Rapp and Manhart [33]. Relatively to the experimental data, it appears that the PITM1 and PITM2 simulations predict a too large recirculation zone whereas the PITM3 and PITM4 simulations return a better estimate. More precisely, the PITM3 and PITM4 simulations provide separation and reattachment points that agree very well with the experimental data while the PITM1 and PITM2 simulations slightly overpredict both the separation and reattachment points. The reason of this noticeable difference in the recirculation zone between these four simulations and in particular in the misprediction of the reattachment point may remain questionable at a first glance. But as a result when comparing the mesh resolutions between these simulations, and particularly the results associated with the PITM2 and PITM3 simulations, there is no doubt that the grid resolution in the spanwise direction is the clue to understand this outcome. Indeed, it appears that the PITM1 behaves like the PITM2 simulation whereas the PITM3 behaves like the PITM4 simulation. Both the PITM3 and PITM4 simulations are performed on meshes with the same resolution in the spanwise dimension. The spanwise resolution is indeed well identified in LES to play an important role in the vortex-streaks mechanism of wall turbulence and therefore in the determination of the flow structure. It is also significant to address the spatial extent of the recirculation bubble itself, determined as the regions in which the mean velocity profile contains negative longitudinal component of velocity. The upstream and downstream values denoted $(x_1/h)_{b1}$ and $(x_1/h)_{b2}$ respectively are included in Table 1 together with the bubble length. Note that the streamwise locations denoted $(x_1/h)_{sep}$ and $(x_1/h)_{reat}$ correspond to the usual separation and reattachment points in which the friction factor vanishes while the locations $(x_1/h)_{b1}$ and $(x_1/h)_{b2}$ denote the upstream and downstream limit positions of the main central recirculation bubble for which no inflection point appear in the streamline contour. These limits are defined by the location of the vertical tangent in the front and in the rear of the bubble. From this bubble length, it appears then that the grid simulations PITM1 and PITM2 behaves more or less like the RSM numerical modeling while the other grid simulations PITM3 and PITM4 shows improvement. This result is both expected and surprising ! First at all, it is expected because the modeled part in the PITM1 simulation is larger than in the PITM4 simulation and so the inheritance from the RSM is also larger. So, if the use of stress transport equations as a subfilter model is indeed beneficial when the filter cutoff is located before the inertial spectral zone, some loss of accuracy happens

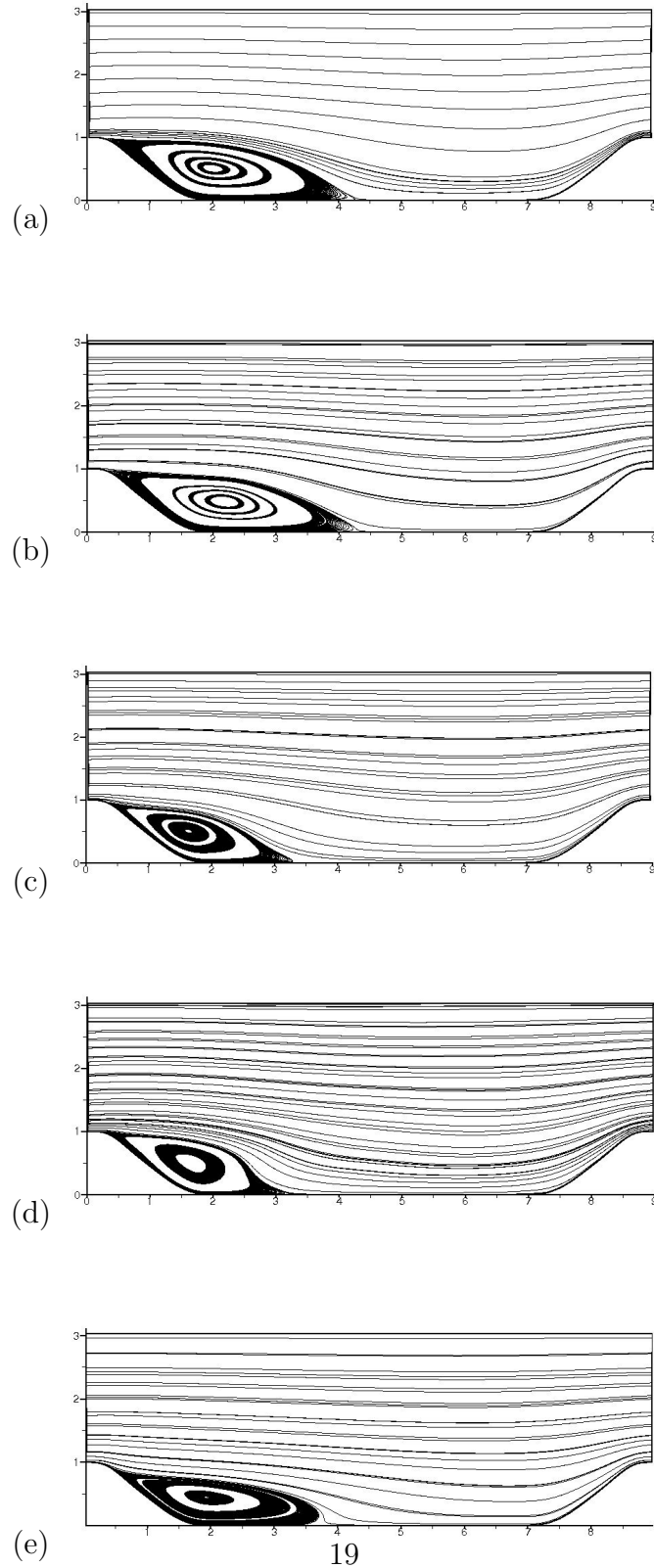


Figure 4. Streamlines of the average flowfield at $Re = 37000$. (a) PITM1 ($80 \times 30 \times 100$). (b) PITM2 ($160 \times 30 \times 100$). (c) PITM3 ($80 \times 60 \times 100$). (d) PITM4 ($160 \times 60 \times 100$). (e) RSM ($80 \times 30 \times 100$).

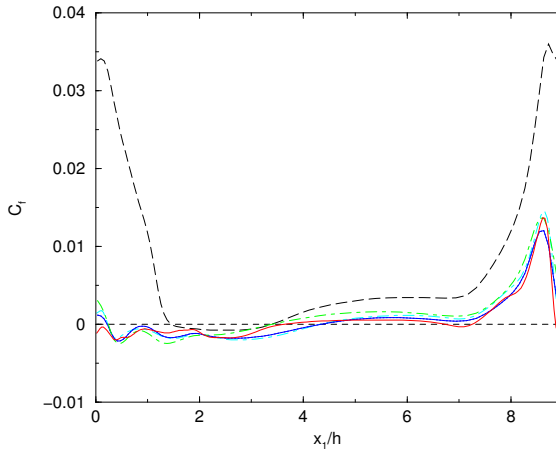


Figure 5: Friction coefficient $C_f = \tau_w / (0.5\rho U_b^2)$ along the lower wall at $Re = 37000$. PITM1 ($80 \times 30 \times 100$) \cdots ; PITM2 ($160 \times 30 \times 100$) $-\ -$; PITM3 ($80 \times 60 \times 100$) $-\cdot-$; PITM4 ($160 \times 60 \times 100$) $—$; RSM computation $—$ ($80 \times 30 \times 100$).

when the simulation runs too close to statistical modeling. The grids of the mesh may appear too coarse to accurately capture the three-dimensional effects. But this result is surprising because the meshes associated with the PITM2 and PITM3 simulation contain both the same number of grid points (1/4 million) and that the modeled energy between these two simulations is roughly of the same order. This last point will be studied in figure 12. So that the only change between the PITM2 and PITM3 simulation lies in the spanwise resolution which is different. Regarding the RANS modeling, it is found that the recirculation zone is strongly under-predicted in comparison with those measured from the experiment, mainly because the separation is delayed. The modeling of the low Reynolds number wall layer is probably involved in this finding. Note that the authors have checked the grid independence solution for the RANS computation which is not presented here for the sake of simplicity of presentation. As for the flow computed at the lower Reynolds number $Re = 10595$ [7], this RSM misprediction is likely to be due to the RANS modeling itself that relies on statistical means equivalent to a long-time averaging. Because of this assumption, this method is not able to capture the effect of instantaneous eddies issued from the streamwise curvature of the lower wall. The occurrence of separation is noticeably delayed downstream. The comparisons in the separated zone length and the recirculation bubble length made in this section between predicted values from the simulations and the measured ones deserve interest in order to get an appraisal of the PITM potential. However, on the physical point of view, it can be noted that some uncertainty remains and that no definite conclusion can be drawn from these comparisons. Indeed, if one refers to the flow computed in the same geometry but at the lower Reynolds number $Re = 10595$, the highly resolved LES performed by Breuer et al. [31] on a very refined mesh ($13.1 \cdot 10^6$ grid points) which constitutes the reference simulation for this benchmark has returned a reattachment point at $x_1/h = 4.694$ whereas the experiment conducted by Rapp and Manhart [33] using PIV measurements has lead to the value 4.21. The origin of the slight discrepancies between these two values is not clear and raises some still open questions.

Experiment /Simulation	Grid points	$(x_1/h)_{sep}$	$(x_1/h)_{reat}$	Separated length	$(x_1/h)_{b1}$	$(x_1/h)_{b2}$	Recirculation bubble length
Exp [33]		0.05	3.76	3.71			
RSM	$2.5 \cdot 10^5$	0.50	4.00	2.15	0.70	3.70	3.00
PITM1	$2.5 \cdot 10^5$	0.19	4.30	4.11	0.50	4.20	3.70
PITM2	$5.0 \cdot 10^5$	0.24	4.26	4.02	0.40	4.20	3.80
PITM3	$5.0 \cdot 10^5$	0.29	3.54	3.25	0.40	3.00	2.60
PITM4	10^6	0.05	3.68	3.63	0.40	2.80	2.40

Table 1: Simulations of flow over periodic hills at $Re = 37000$ including separation, reattachment locations and bubble length.

6.3 Friction coefficient

Figure 5 displays the distribution of the friction coefficient $C_f = \tau_w / (0.5\rho U_b^2)$ along the lower wall for all PITM simulations together with the statistical computation. This information complements the analysis made in the previous section by showing another indicator for separation reattachment phenomena. Some deviations between these different curves are particularly observed in the leeward region of the upstream hill. As a result of interest, one can see that all PITM simulations performed on the coarse and medium meshes yield similar evolutions with a rather good location of the detachment and reattachment points for the PITM3 and PITM4 simulations while the PITM1 and PITM2 simulations show some delay in the location of reattachment point. For all PITM simulations, the friction coefficient decreases rapidly in the windward region of the first hill reaching a first minimum value at $x_1/h \approx 0.40$. From there, the friction increases again towards zero and then undergoes small oscillations to attain a new local minimum at $x_1/h \approx 2.61$ that corresponds roughly to the location of the maximum reverse flow. Afterward, the friction coefficient slowly reincreases towards the second hill crest passing through zero at the reattachment point at $x_1/h \approx 4.30$ and 3.68 for all simulations. Finally, it reaches its maximum value shortly before the second hill crest at $x_1/h \approx 8.56$ where the flow strongly accelerates. On the other hand, it appears that the friction coefficient associated with the RSM computation strongly deviates from the PITM3 and PITM4 results. In particular, the separation point is delayed far downstream, leading to a too short length-scale of the separated zone. Moreover, the friction coefficient is highly over-predicted when moving from the reattachment point to the windward region of the second hill. This study confirms the analysis made in the preceding section suggesting that the full statistical RSM treatment is not sufficient to accurately predict such a type of flow.

6.4 Mean velocities

Figures 6 exhibits the mean velocity profiles $\langle u_1 \rangle / U_b$ at six cross stations $x_1/h = 0.05, 0.5, 2, 4, 6$ and 8 including available experimental profiles [33]. The selected positions encompass the regions in the entrance of the channel $x_1/h = 0.05$, just upon separation $x_1/h = 0.5$, in the middle of the recirculation zone close to the leeward hill face $x_1/h \approx 2$, prior to the reattachment $x_1/h = 4$, the

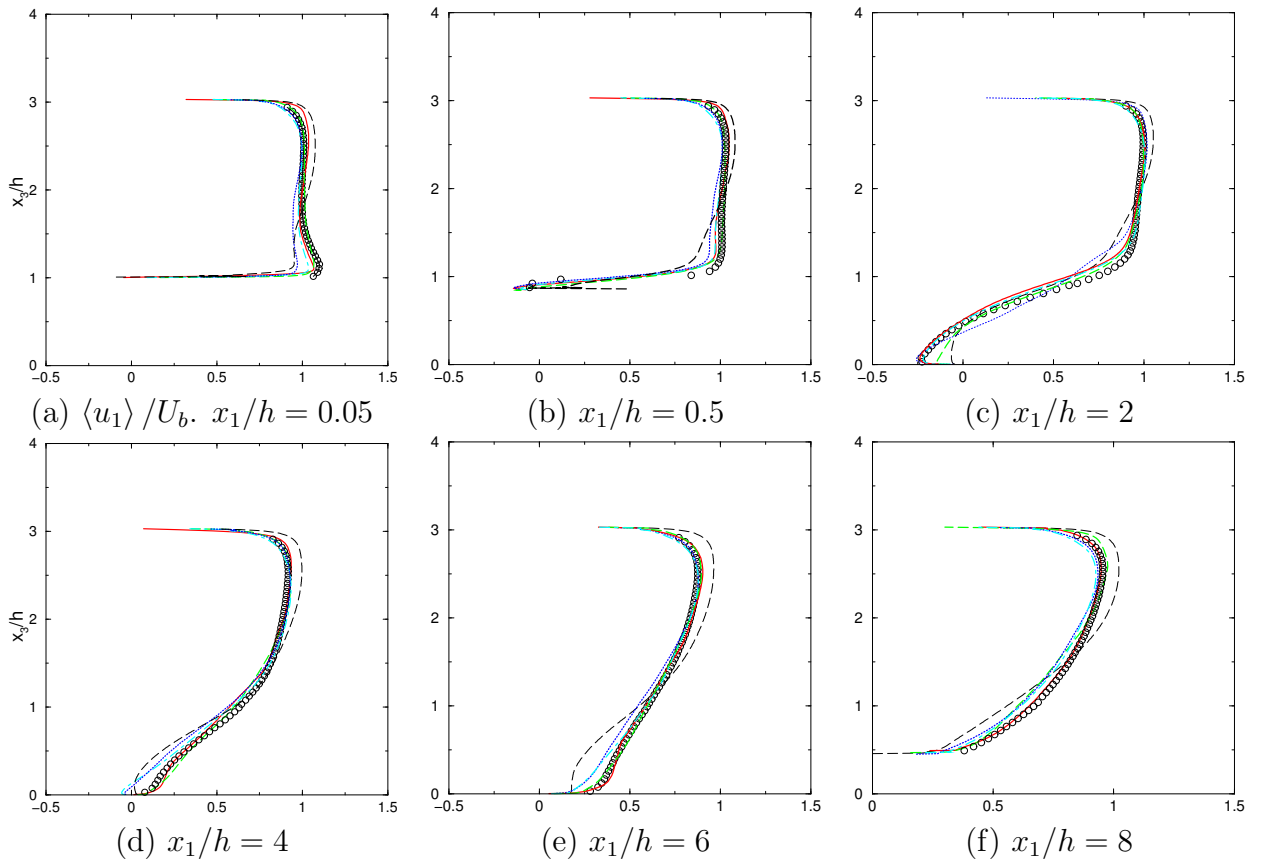


Figure 6. Streamwise velocity $\langle u_1 \rangle / U_b$ at different locations ($x_1/h = 0.05, 0.5, 2, 4, 6, 8$). Experiment \circ (Rapp et al., 2009) $Re = 37000$; PITM1 ($80 \times 30 \times 100$) \cdots ; PITM2 ($160 \times 30 \times 100$) $---$; PITM3 ($80 \times 60 \times 100$) $-\cdot-$; PITM4 ($160 \times 60 \times 100$) $—$; RSM computation $—$ ($80 \times 30 \times 100$).

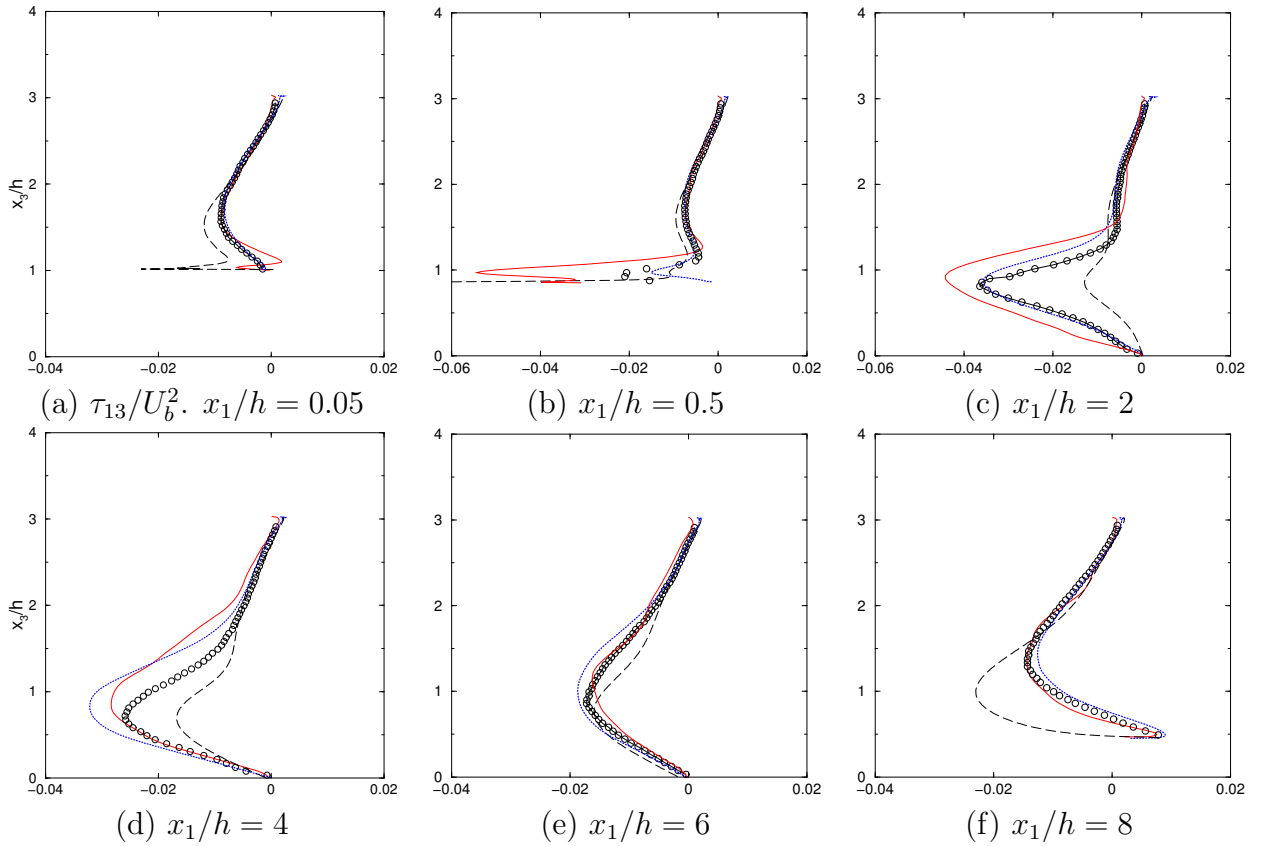


Figure 7. Turbulent shear stress τ_{13}/U_b^2 at different locations ($x_1/h = 0.05, 0.5, 2, 4, 6, 8$). Experiment \circ (Rapp et al., 2009) $Re = 37000$; PITM1 ($80 \times 30 \times 100$) \cdots ; PITM4 ($160 \times 60 \times 100$) \cdots ; RSM $---$

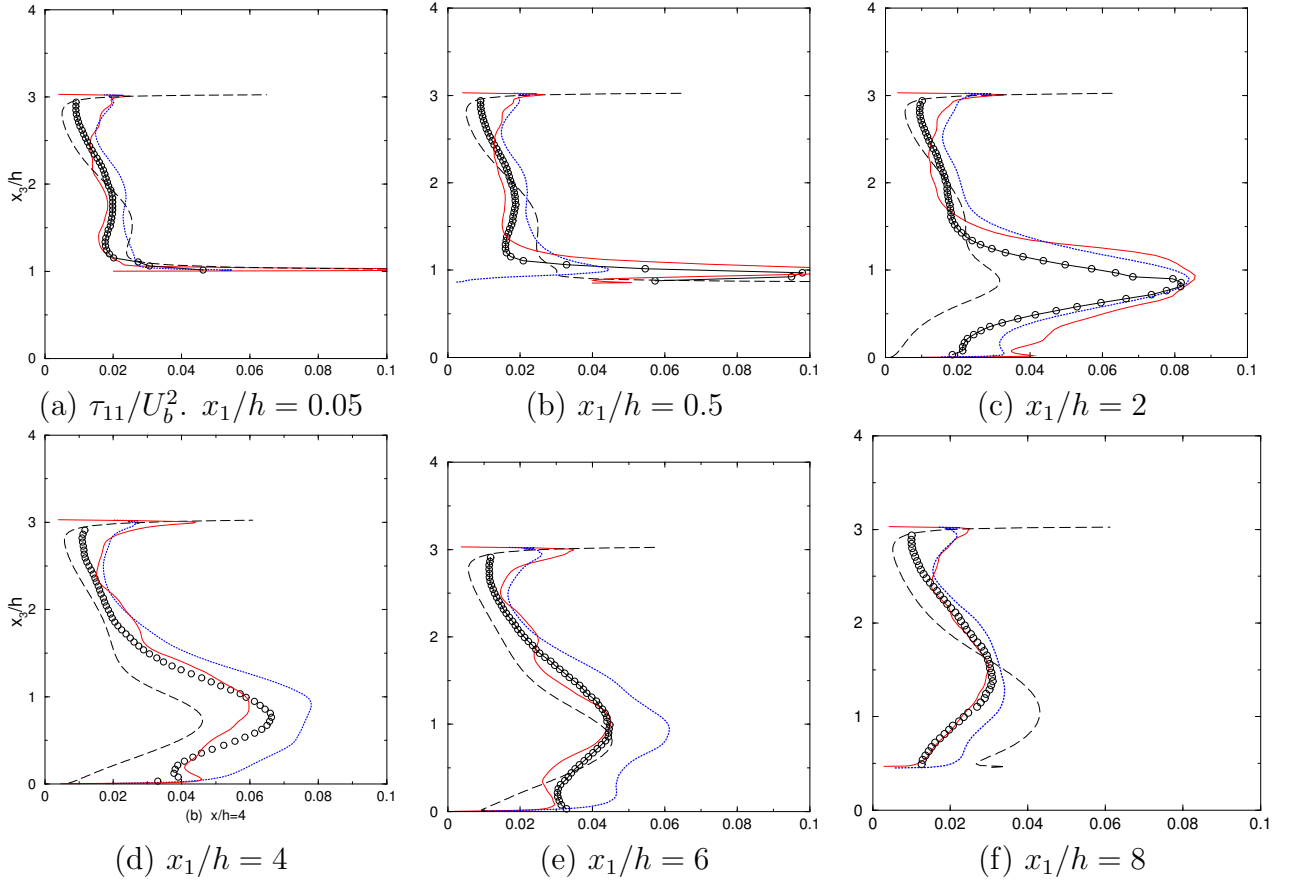


Figure 8. Streamwise turbulent energy τ_{11}/U_b^2 at different locations ($x_1/h = 0.05, 0.5, 2, 4, 6, 8$). Experiment \circ (Rapp et al., 2009) $Re = 37000$; PITM1 ($80 \times 30 \times 100$) \cdots ; PITM4 ($160 \times 60 \times 100$) \cdots ; RSM $- -$

post-reattachment and flow recovery $x_1/h = 6$, and finally, the region of accelerating flow on the windward slope of the hill $x_1/h = 8$. At the position $x_1/h = 0.05$, the streamwise velocity features a near-wall peak due to the preceding flow acceleration along the windward of the hill which is more and more pronounced as the Reynolds number Re increases [33]. Recent studies suggest that this overshoot in the velocity should be attributed to inviscid effects [33, 48] rather than to turbulent effects. At the position $x_1/h = 2$, the velocity near the wall is negative showing that the boundary layer is detached (except for the RANS-RSM calculation). The maximum reverse flow occurs in this region. In the post reattachment region after $x_1/h = 4$, the flow consists of the boundary layer which develops from the reattachment point and the wake originates from the separated shear layer further upstream. At the position $x_1/h = 8$, the flow is strongly accelerated due to the presence of the second hill. One can see that the mean velocity profiles returned by the PITM4 simulation exhibit a very good agreement with the reference data at almost each position except perhaps at $x_1/h = 2$. In particular, this simulation accurately captures the overshoot directly above the hill

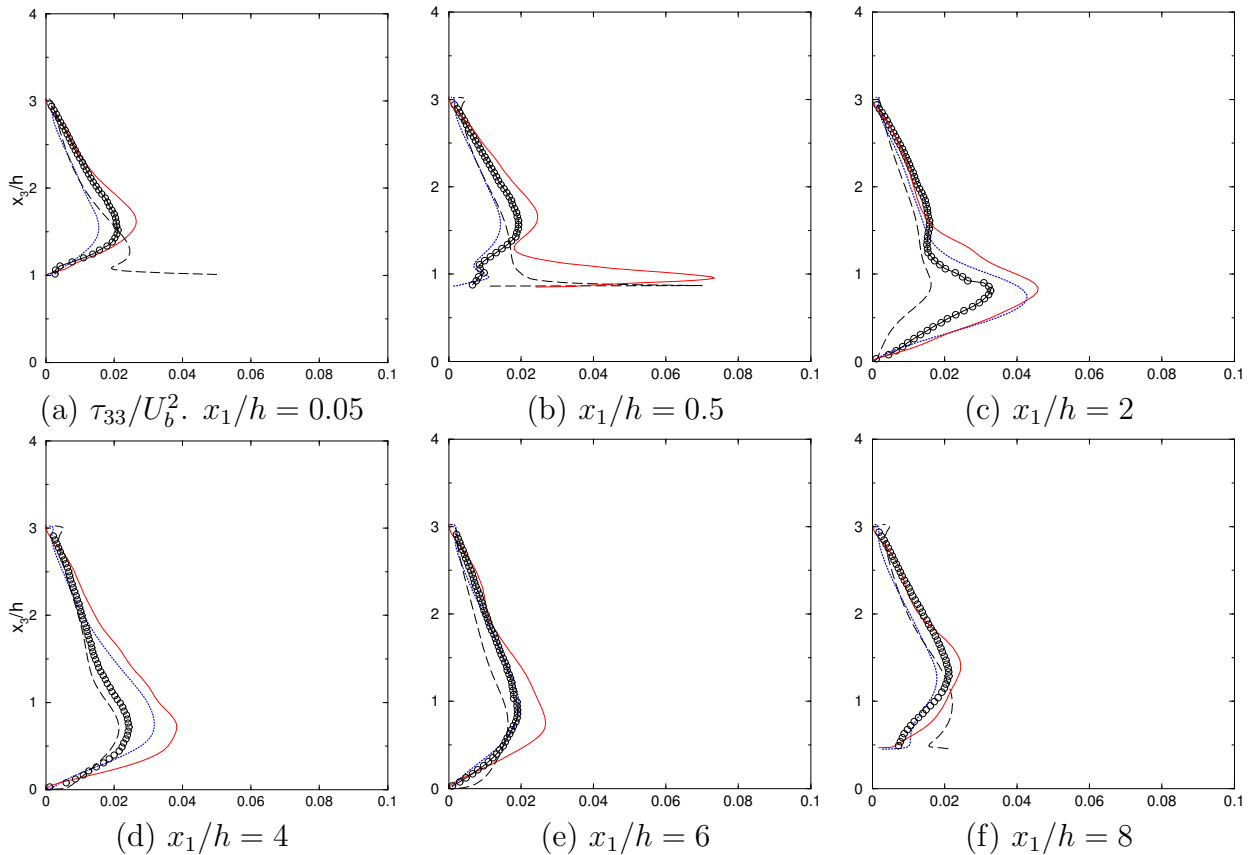


Figure 9. Turbulent energy in the normal direction to the walls τ_{33}/U_b^2 at different locations ($x_1/h = 0.05, 0.5, 2, 4, 6, 8$). Experiment \circ (Rapp et al., 2009) $Re = 37000$; PITM1 ($80 \times 30 \times 100$) \cdots ; PITM4 ($160 \times 60 \times 100$) \cdots ; RSM $--$

crest at $x_1/h = 0.05$ which is very difficult to reproduce numerically [48]. The mean velocity profiles at the sections $x_1/h = 4$ and $x_1/h = 6$ where the flow reattaches are remarkably well recovered in accordance with the experimental data. Only very slight discrepancies are observed in the immediate vicinity of the upper wall. Overall, the mean velocity profiles predicted by the PITM1 and PITM2 simulations performed on the coarse and medium grids show not too bad agreement with the reference data, although some discrepancies are clearly visible at almost each section and particularly at $x_1/h = 0.05, 4$ and 6 . It appears that these first two simulations PITM1 and PITM2 are not really able to capture the overshoot that occurs in the boundary layer of the lower wall at $x_1/h = 0.05$. As it was seen, both the PITM3 and PITM4 simulations provide much better results than the PITM1 and PITM2 simulations because of the mesh refinement in the spanwise direction. The question is then to confirm the influence of the streamwise and spanwise grid resolution, respectively, on the solution. The answer to the above question is given by mean velocity profiles associated with the PITM2 and PITM3 simulations. The mean velocity profiles returned by the PITM3 and PITM4 are sensibly the same and agree very well with the experimental data in almost

all the sections, even if some slight differences are however visible at the locations $x_1/h = 2$ and $x_1/h = 8$ for instance. In particular, the flow region in the lower wall is perfectly well reproduced in agreement with the data although the meshes associated with the PITM3 and PITM4 simulation are of coarse resolution (1/2 and 1 million grid points) in comparison with the those required for performing highly resolved LES (at least 3.8 millions grid-points as indicated in reference [48]). Figure 6 also confirms that the PITM1 and PITM2 simulations yield both similar mean profiles despite the mesh is more refined in the longitudinal direction for the PITM2 (160 grids points instead of 80 grid points). If the PITM1 and PITM2 simulations do return acceptable velocity profiles from a practical engineering point of view, while the PITM3 and PITM4 provide very good ones, on the other hand, the RSM computation yields several weaknesses in the predicted results on several aspects that show evident discrepancies with the reference data. Firstly, the flatness of the mean velocity due to the turbulence effects is not well reproduced. Secondly, the boundary layer on the lower wall is mispredicted in most stations of the channel and particularly at $x_1/h = 6$. As it was observed in the preceding sections, the flow computed by the RSM reattaches too early at the lower wall at the station $x_1/h = 3.60$ indicating that the RSM model does not succeed in reproducing satisfactorily the recovery process. At this location $x_1/h = 3.60$, the boundary layer thickness is underpredicted by the RSM model. The origin of the observed discrepancies with the experimental data is not clear unless to point out that this type of flow is essentially governed by unsteady mechanisms of separation and reattachment of the boundary layer in which very large three-dimensional eddying motions are very important. These cannot be correctly mimicked by fully statistical RANS models, even if using sophisticated models like advanced second-moment closures. Finally, relatively to the flow previously studied at $Re = 10595$ [7, 40], it appears that the RSM prediction deteriorates as the Reynolds number Re increases from 10595 to 37000 confirming that high Reynolds number effects are very difficult to reproduce numerically.

6.5 Turbulent stresses

The authors have checked that the PITM2 behaves like PITM1, and that the PITM3 behaves like PITM4, and that the mean velocity and turbulent profiles returned by PITM1, PITM2, on the one hand, and PITM3, PITM4, on the other hand, are almost the same. So that, to alleviate the presentation of the following figures, only the profiles associated with the the PITM1, PITM4 simulations and RSM computation which substantially differ from each other are discussed in this section. The total stresses τ_{ij} are obtained as the sum of the mean subfilter and resolved parts as indicated in equation (8). Figure 7 shows the turbulent shear stress τ_{13}/U_b^2 profiles at different positions of the channel. Overall, one can see that the shear stress profiles returned by both PITM simulations present a quantitative good agreement with the reference data. Relatively to the PITM1 profiles, the PITM4 profiles are marked by a turbulent peak occurring at $x_1/h = 0.05$ and especially at $x_1/h = 0.5$, peak which is not measured by the experimental device. Globally, the agreement between the PITM profiles and the experimental data is very encouraging considering simulations performed on such coarse grids. If these results show a remarkably good degree of agreement, it appears on the contrary that the shear stress returned by the statistical RSM model highly deviate from the reference data in most positions of the channel. The shear stress is over-predicted in the windward regions of the hill crest at the stations $x_1/h = 0.05$ and 8, and under-

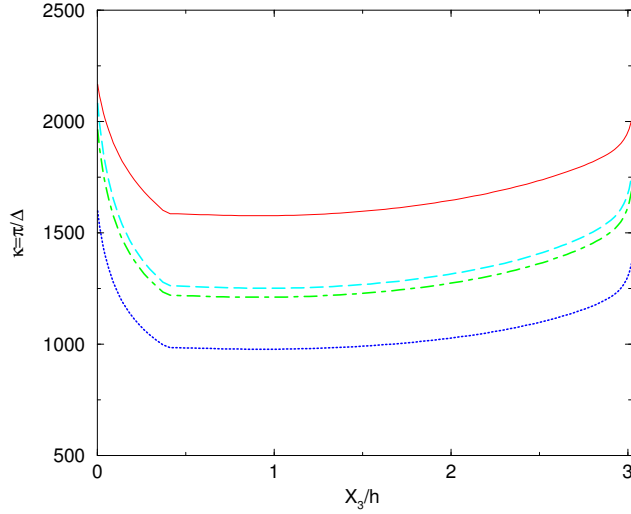


Figure 10: Cutoff wave number versus the normal direction to the wall at the location $x_1/h = 4$. PITM1 ($80 \times 30 \times 100$) \cdots ; PITM2 ($160 \times 30 \times 100$) $---$; PITM3 ($80 \times 60 \times 100$) $-. -.$; PITM4 ($160 \times 60 \times 100$) $---$;

predicted in the stations in the leeward regions at $x_1/h = 2$ and 4 but surprisingly, almost agrees with the experimental data in the stations $x_1/h = 0.5$ and 6. Figures 8 and 9 display the profiles of the streamwise and vertical turbulent normal stresses τ_{11}/U_b^2 and τ_{33}/U_b^2 , respectively, at the same successive locations. A first sight to the figure plots reveals that the turbulent stresses returned by the PITM simulations agree fairly well with the experimental profiles for almost all positions even if some slight discrepancies with the data still remain for the PITM1 simulation. The agreement with the data for the PITM4 stress profiles is even more satisfying. As for the turbulent shear stress, the normal stresses predicted by the PITM4 simulation present a turbulent peak in the boundary layer of the lower wall at the stations $x_1/h = 0.05$ and $x_1/h = 0.5$. In the present case, some of these peaks have been actually measured by the experiment. For instance, the one occurring at the station $x_1/h = 0.5$ for the normal stress τ_{11} is particularly visible and well recovered by the PITM4 simulation. But surprisingly, there is no measured important turbulent peak at the same station $x_1/h = 0.5$ for the stress τ_{22} while the PITM4 simulation has predicted one. On the contrary to PITM simulations, the turbulent stresses returned by the statistical RSM computation show several disagreements with the experimental data even in the shape of the individual profiles.

6.6 Sharing out of the turbulent energy

Figure 10 describes the evolution of the cutoff wave number versus the normal direction to the wall at the location $x_1/h = 4$ for all PITM simulations. The cutoff wave number $\kappa_c = \pi/\Delta$ is computed using the grid filter defined in equation (11) where Δ_a and Δ_b have been considered to handle anisotropic grids. As a result, all PITM curves present the same evolution but only differ

in regard with the numerical value which is higher for PITM4, lower for PITM1 and almost the same for PITM2 and PITM3. Because of the grid refinement, the cutoff wave number reaches its highest values near the walls and its lower values in the center of the channel. Figure 11 depicts the contours of the ratio of the subfilter viscosity to the molecular viscosity $\mu_{sfs}/\mu = c_\mu \rho k_{sfs}^2 / (\mu \epsilon)$ in the channel for all PITM simulations. One can see that the ratio of viscosities μ_{sfs}/μ is of relatively high values for the PITM1 simulation performed on the very coarse mesh, roughly of the same values for the PITM2 and PITM3 simulations but lower than for the PITM1, while of low values for the PITM4. Moreover, the distribution of energy levels appears more pronounced in the near lower wall region than in the center of the channel according to previous studies [7]. In particular, the level of the viscosity ratio μ_{sfs}/μ is higher in the leeward region of the second hill after the flow reattachment than in the windward region of the first hill before the flow detachment. Note that the color panel levels are the main elements to learn from these plots because the detailed field visualized here is instantaneous. Figure 12 gives the values of the ratio of the subfilter energy to the total energy $\langle k_{sfs} \rangle / k$ for all simulations, PITM1, PITM2, PITM3 and PITM4 at the locations $x_1/h = 0.05, 0.5, 2, 4, 6,$ and 8 . As expected, it appears that the sharing out of the turbulence energy is governed by the filter size (in practice the mesh spacing) in relation with the turbulence length-scale. All of these quantities appear in the definition of the parameter η introduced in the section describing the general PITM formalism. This is merely a consequence of the particular choice of the meshes. This result comes from the fact that the core flow is strongly characterized by the turbulent large scales whereas the wall region is dominated by smaller scales and at the same time the grid-size is smaller in the wall region than in the center of the channel but in a different ratio than the turbulence macroscales. In the PITM concept, the ratio of the modeled energy to the total energy $\langle k_{sfs} \rangle / k$ continuously varies between the two extreme limits, zero and unity. As a result of interest, one can see that the level of the modeled energy associated with the PITM2 simulation performed on the coarse mesh $80 \times 60 \times 100$ is roughly the same as the one associated with the PITM3 simulation $160 \times 30 \times 100$ although the mean flow and turbulence highly differ from one simulation to the other one. This important outcome suggests that it is not only the ratio of the modeled energy to the total energy, as identified as a the key parameter in PITM, that governs the simulation evolving itself between the RANS and LES regimes but also the particular choice of the mesh refinement either in the streamwise direction or in spanwise direction. For each location, one can see that the subfilter turbulent energy is of higher intensity near the upper wall region than in the lower wall region confirming that the PITM behaves more like LES in the lower wall region where the flow is dominated by large scales. Moreover, we have checked that in the recirculation zone, the turbulence length-scale is relatively high so that the reference equilibrium ratio $\langle k_{sfs} \rangle / k$ defined in references [5, 6] becomes lower. Consequently, the model behaves more like LES. Nevertheless, the grid remains adequate because of the larger turbulence length-scale. The differences observed between the lower and higher regions in the evolution of $\langle k_{sfs} \rangle / k$ results from a stronger spectral non-equilibrium turbulence in the lower wall region. In the present case, the refinement in the spanwise direction allows the PITM3 to mimic the acting mechanisms in the turbulent flow that develop because of the three dimensional component, leading to a better flow prediction than the PITM2 simulation which is performed on the mesh including only a refinement in the streamwise direction. Figure 13 displays separately the subfilter and resolved parts of the turbulent shear stress at six locations of the channel for both PITM1 and PITM4 simulations.

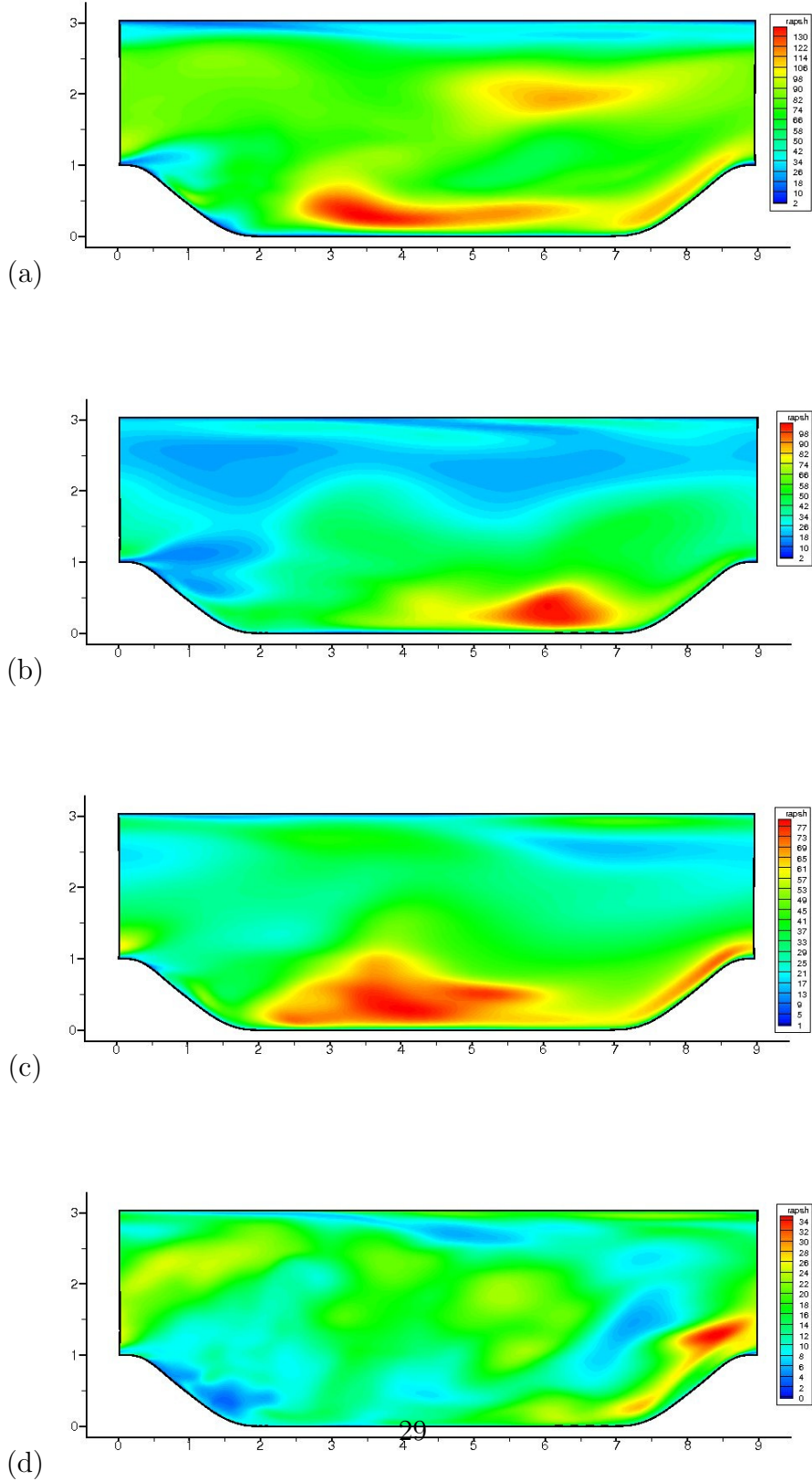


Figure 11 Contours of the ratio of the subfilter viscosity to the molecular viscosity μ_{sf}/μ . (a) PITM1 ($80 \times 30 \times 100$). (b) PITM2 ($160 \times 30 \times 100$). (c) PITM3 ($80 \times 60 \times 100$). (d) PITM4 ($160 \times 60 \times 100$).

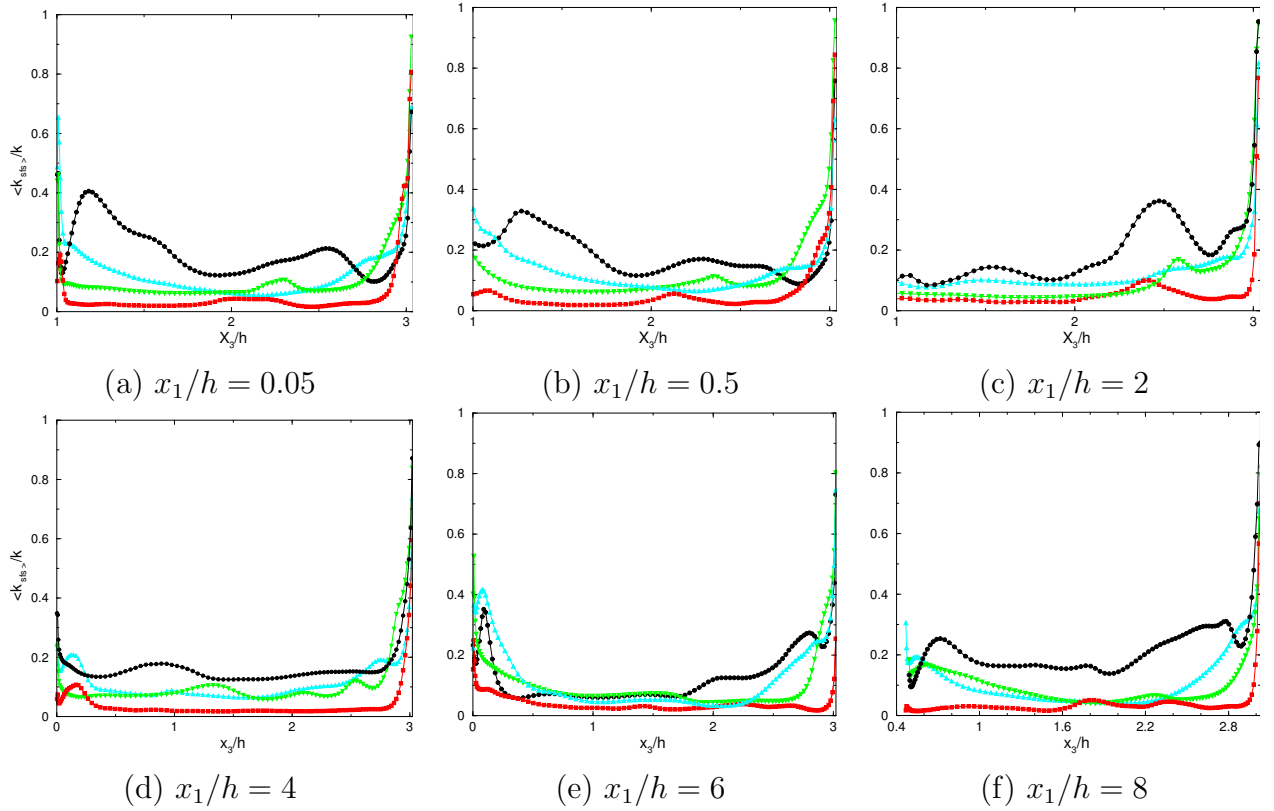


Figure 12. Ratio of the subfilter energy to the total energy $\langle k_{sf_s} \rangle / k$ at different locations ($x_1/h = 0.05, 0.5, 2, 4, 6, 8$). PITM1 ($80 \times 30 \times 100$) \bullet ; PITM2 ($160 \times 30 \times 100$) \blacktriangle ; PITM3 ($80 \times 60 \times 100$) \blacktriangledown ; PITM4 ($160 \times 60 \times 100$) \blacksquare .

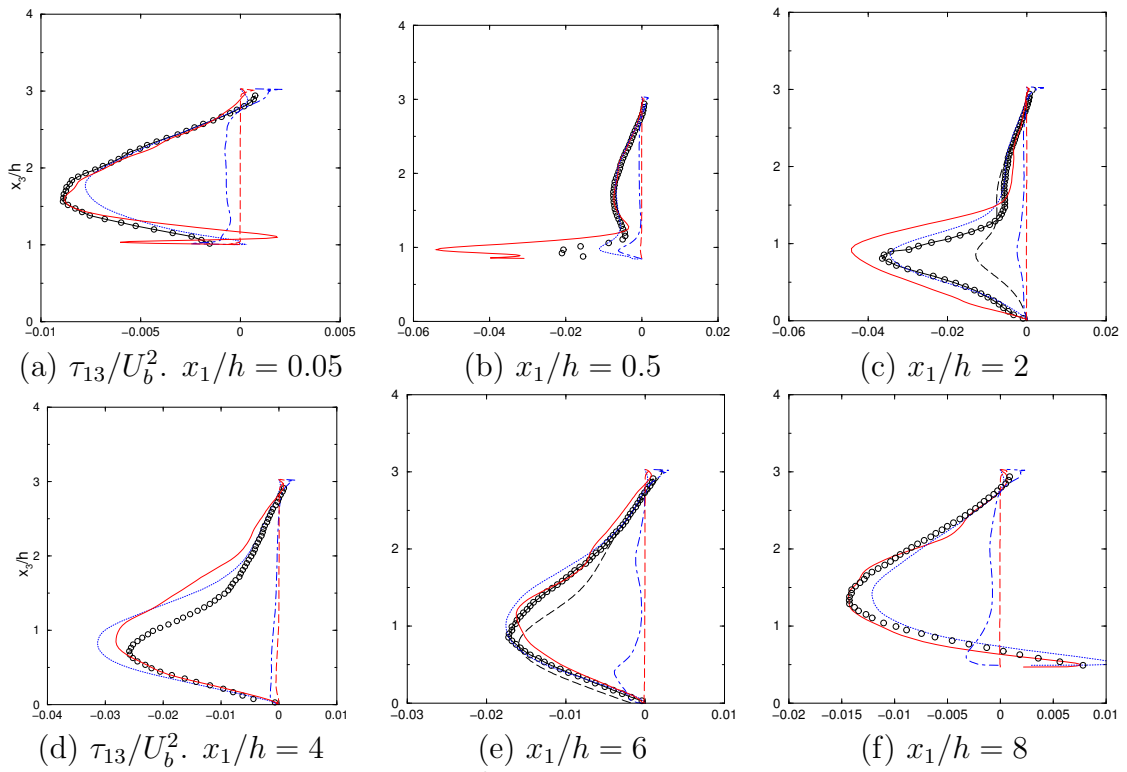


Figure 13. Turbulent shear stress τ_{13}/U_b^2 at different locations ($x_1/h = 0.05, 0.5, 2, 4, 6, 8$). Experiment \circ (Rapp et al., 2009) $Re = 37000$; PITM1 ($80 \times 30 \times 100$), $(\tau_{13})_{sgs}$: $-\cdot-\cdot-$; $(\tau_{13})_{les}$: $\cdot\cdot\cdot\cdot$. PITM4 ($160 \times 60 \times 100$), $(\tau_{13})_{sgs}$: $-\cdot-\cdot-$; $(\tau_{13})_{les}$: $-\cdot-$.

For the PITM4, one can see that the subfilter part reduces to zero apart from small subfilter contributions near the wall regions while for the PITM1, both contributions, modeled and resolved parts, are appreciable even if the subfilter part is lower than the the resolved one.

6.7 Flow anisotropy

Figure 14, 15 and 16 describe the solution trajectories along vertical lines starting from the lower wall towards the upper wall at different streamwise locations, that are projected onto the second and third invariants plane formed from the subfilter, resolved and total anisotropy tensors, respectively. In this framework, Lumley [34] has indicated that the possible states of turbulence must remain inside a curvilinear triangle delimited by the straight line of the two-dimensional state satisfying equation $A_3 - A_2 + 8/9 = 0$ and by two limiting curves of axisymmetric states of equations $|A_2| = 6^{1/3} A_3^{2/3}$. For isotropic flows, we recall that the flatness parameter A goes to unity since the invariants A_2 and A_3 are zero whereas near the walls, A is close to zero because of the two component limit turbulence states. Each diagram of these figures at the stations $x_1/h = 0.05, 0.5, 2, 4, 6$ and 8 shows that the solution trajectories do remain inside the curvilinear triangle of realizability, confirming that the realizability conditions associated with the subfilter, resolved and total or Reynolds stresses [55] are well satisfied. For the subfilter scale stresses, this result was expected since it has been demonstrated in reference [23] that the present subfilter scale stress model satisfies the weak form of the realizability conditions from a physical standpoint [42]. In that sense, the solutions trajectories plotted in each diagram of figure 14 allow to verify this point in some particular cross sections of the channel. The fact that these conditions are also satisfied for the resolved and total stress tensors simply means that the turbulent energy initially splitted into modeled and resolved parts can be fairly well reconstructed as a whole from each different contributions of energy according to the physics of turbulence. Let us now analyze the solutions trajectories in the realizability triangle projected onto the plane formed by the second and third invariants of the subfilter scale anisotropy $(a_{ij})_{sfs} = [\langle(\tau_{ij})_{sfs}\rangle - \frac{2}{3} \langle k_{sfs} \rangle \delta_{ij}] / \langle k_{sfs} \rangle$. From figure 14, one can see that the trajectories start from the straight line of two-component limit corresponding to the lower or the upper wall regions and these curves reach a more isotropic state near the origin of the diagram associated with the centered region of the channel. As a result of interest, it appears that the flow anisotropy resulting from the subfilter part of the turbulent energy observed all along its trajectory is more pronounced near the upper wall than near the lower wall. This outcome is not surprising since the lower boundary layer is modified by the wake of the flow which has separated from the first hill. The solutions trajectories computed from the resolved anisotropy tensor $(a_{ij})_{les} = [\langle(\tau_{ij})_{les}\rangle - \frac{2}{3} \langle k_{les} \rangle \delta_{ij}] / \langle k_{les} \rangle$ are represented on Figure 15. As for the subfilter anisotropies viewed in figure 14, one can remark that the resolved anisotropies trajectories computed from the resolved scales still lie within the curvilinear triangle implying also that the constraints of realizability are satisfied. But the solution trajectories differ from one diagram to another one, suggesting that the flow anisotropy strongly varies in space when moving from the windward region of the first hill at $x_1/h = 0.05$ to the leeward region of the second hill at $x_1/h = 8$. In the sections located at $x_1/h = 4$ and $x_1/h = 6$, the anisotropy is more pronounced than in the other sections. Figure 15 indicates also that the resolved anisotropy tensor is of lower intensity in the recirculation zone at $x_1/h \approx 2$ than in the reattachment zone at $x_1/h \approx 4$ where the wall

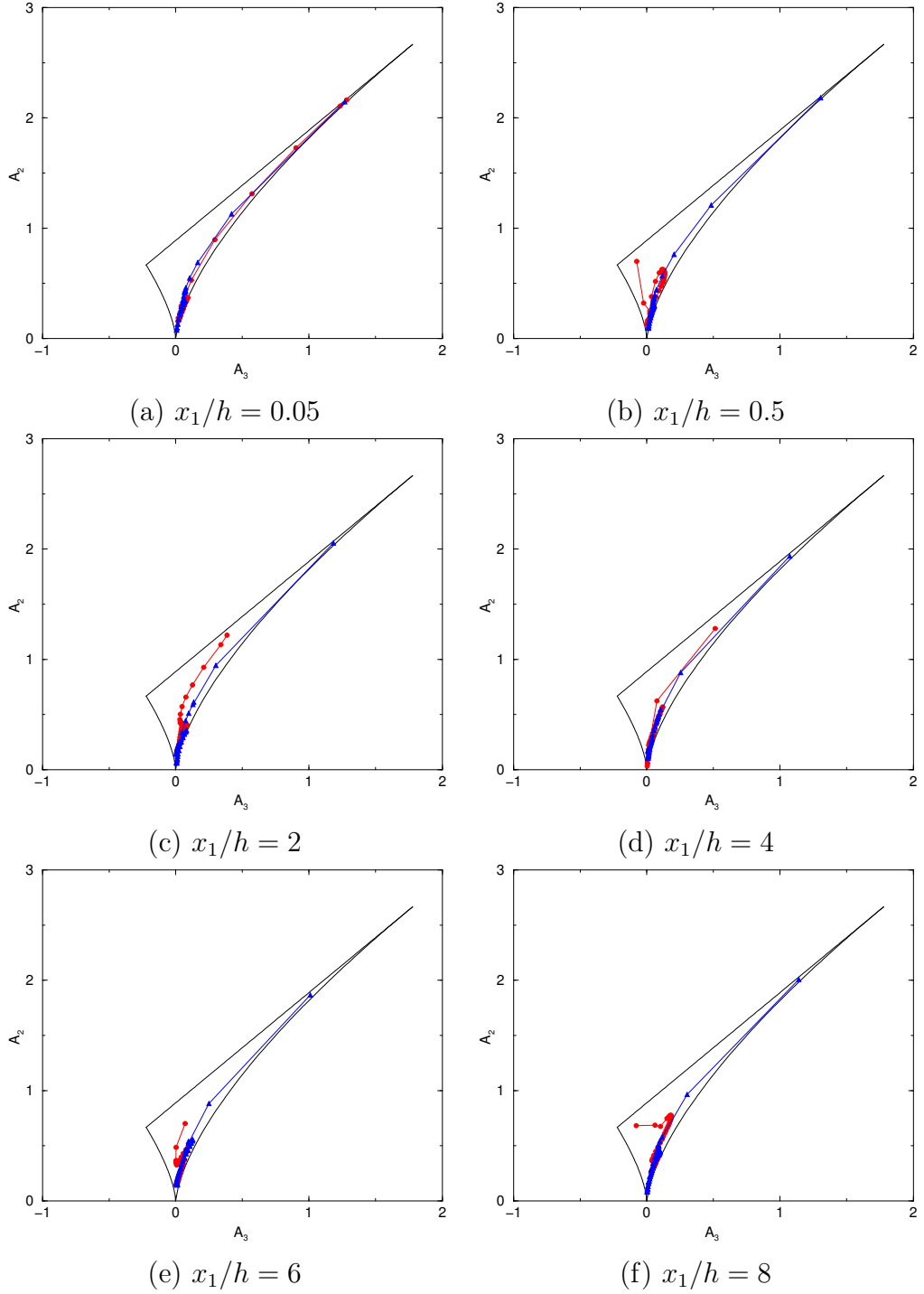


Figure 14. Solutions trajectories along vertical lines at different locations ($x_1/h = 0.05, 0.5, 2, 4, 6, 8$) projected onto the second-invariant/third-invariant plane formed by the subfilter scale anisotropy tensor $(a_{ij})_{sfs} = [\langle (\tau_{ij})_{sfs} \rangle - \frac{2}{3} \langle k_{sfs} \rangle \delta_{ij}] / \langle k_{sfs} \rangle$ ● lower wall; ▲ upper wall. PITM1 ($80 \times 30 \times 100$)

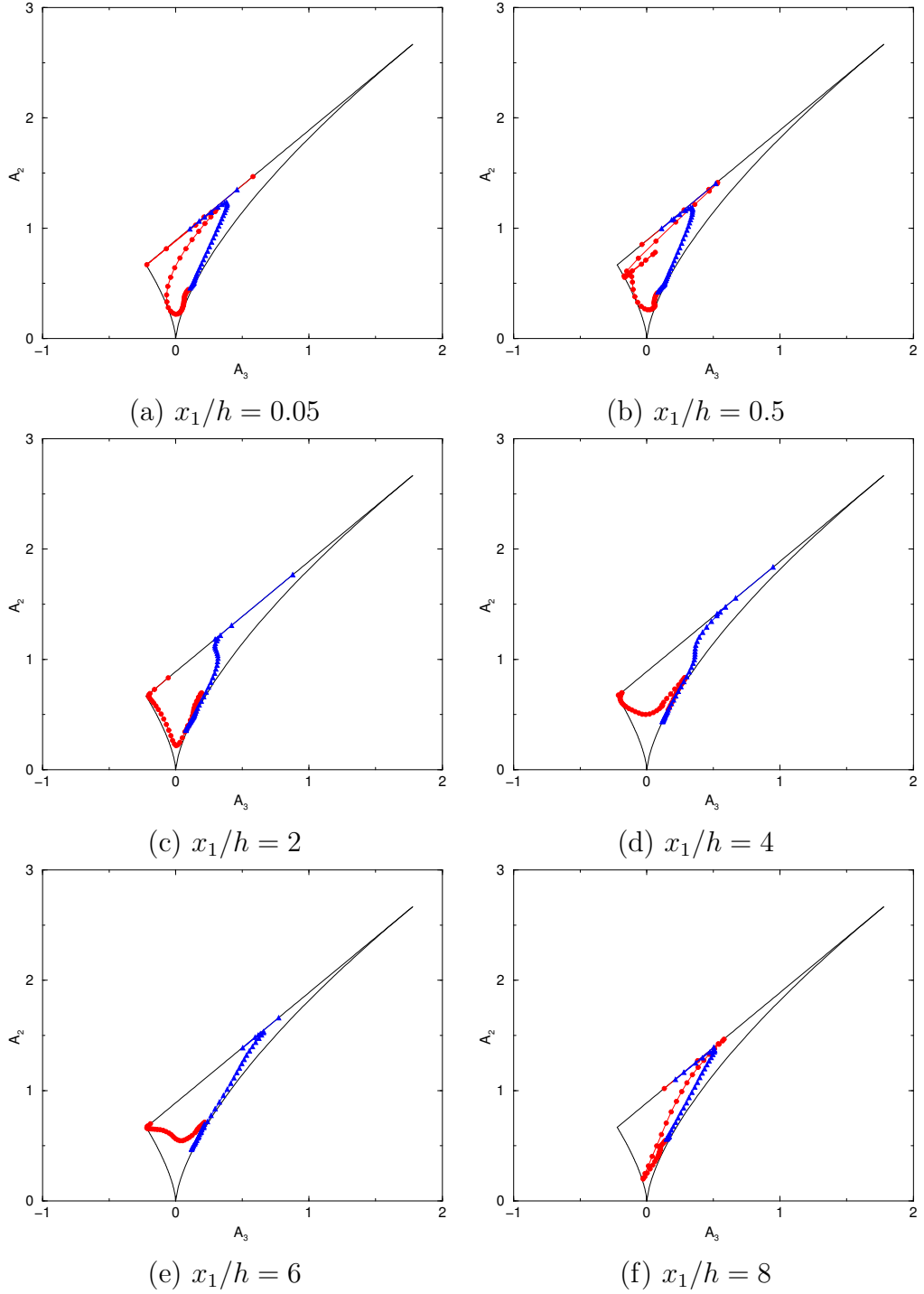


Figure 15. Solutions trajectories along vertical lines at different locations ($x_1/h = 0.05, 0.5, 2, 4, 6, 8$) projected onto the second-invariant/third-invariant plane formed by the resolved scale anisotropy tensor $(a_{ij})_{les} = [\langle(\tau_{ij})_{les}\rangle - \frac{2}{3}\langle k_{les}\rangle\delta_{ij}]/\langle k_{les}\rangle$ • lower wall; ▲ upper wall. PITM1 ($80 \times 30 \times 100$)

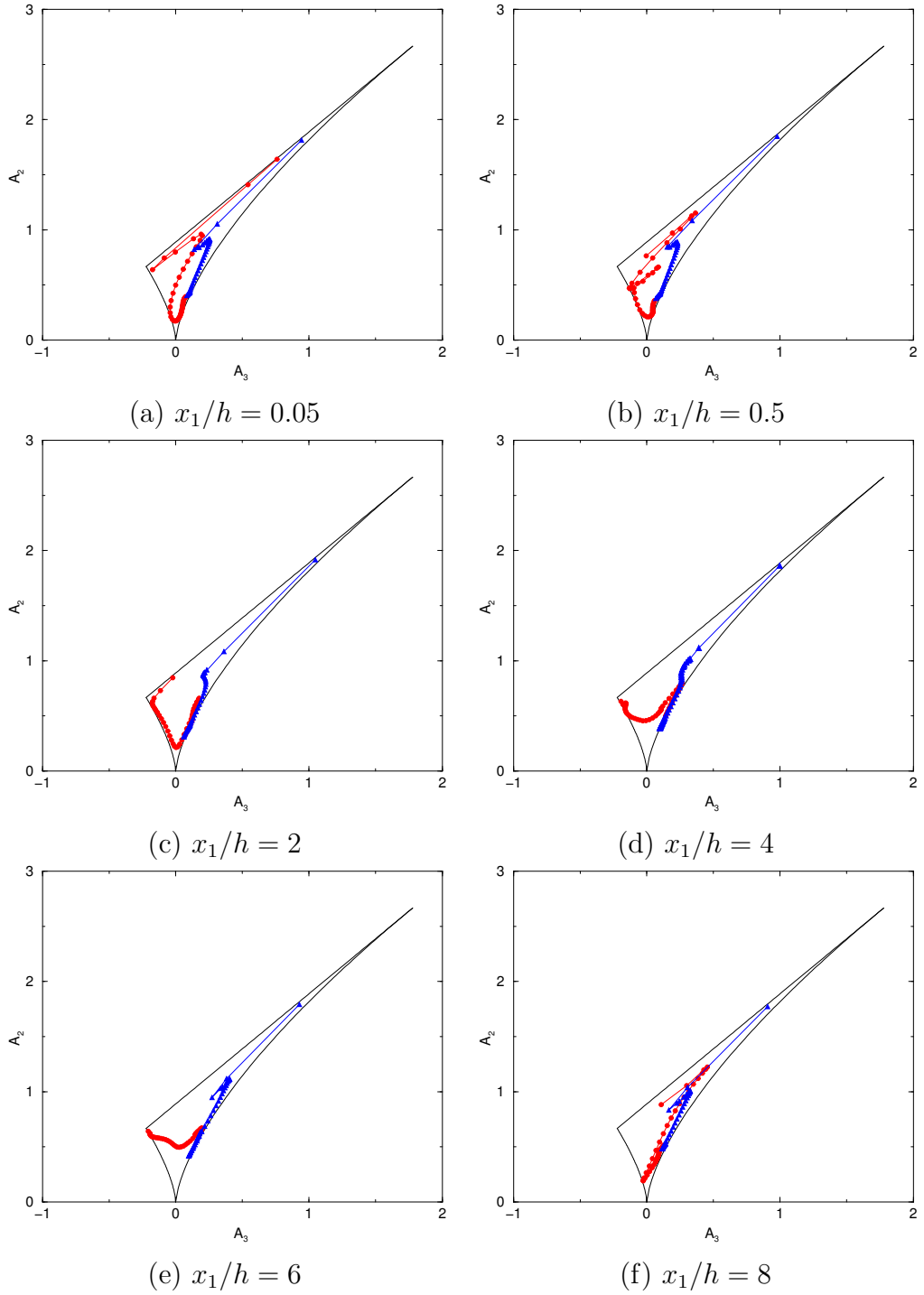


Figure 16. Solutions trajectories along vertical lines at different locations ($x_1/h = 0.05, 0.5, 2, 4, 6, 8$) projected onto the second-invariant/third-invariant plane formed by the anisotropy tensor $a_{ij} = (\tau_{ij} - \frac{2}{3}k\delta_{ij})/k$. \bullet lower wall; \blacktriangle upper wall. PITM1 ($80 \times 30 \times 100$)

effects are more pronounced. The solution trajectories computed from the total anisotropy tensor $a_{ij} = (\tau_{ij} - \frac{2}{3}k\delta_{ij})/k$ are then shown in figure 16. These trajectories can be compared with those computed by Frohlich et al. [30] when performing highly resolved LES, the subfilter part in their case being neglected in comparison with the resolved one. As a result, one can see that the present trajectories compare very well with those plotted in figure 16 of reference [30] at the cross sections $x_1/h = 0.50, 2, 6$ and 8 although some minor differences can be however observed in the immediate vicinity of the walls, as for instance for the trajectories computed at $x_1/h = 6$. As a consequence, this section demonstrates in some particular cases that the PITM simulation is able to reproduce the flow anisotropy in the whole channel as well as to satisfy the realizability conditions [55].

6.8 Energy spectrum densities

An example of the time evolution of the instantaneous velocity components $u_1^<$, $u_2^<$ and $u_3^<$ is given in figure 17. This plot displays the time signal recorded during the time interval corresponding to roughly six convective time scale $T = D_1/U_b$ taken in the center of the recirculation zone at the point of coordinates $x_1/h = 2$, $x_3/h = 0.5$ located in the mid-plane $x_2/h = 2.25$ in the spanwise direction. In this flow recirculation zone, note that the mean velocity is close to zero $\langle u_1 \rangle \approx \langle u_2 \rangle \approx \langle u_3 \rangle \approx 0$. At a first sight, it can be seen that the recorded signal presents very low frequencies undulations of the order of $\nu = 1/0.01 \approx 100$ Hz, or in dimensionless frequency normalized by the bulk velocity U_b and the channel height h , $\nu^* = \nu h/U_b \approx 0.13$, that are similar to those observed in figure 18 of reference [30] but at the lower Reynolds number $Re = 10595$. This frequency corresponds to the return time of the turbulent large eddies and its order of magnitude is roughly the same as the characteristic frequency obtained assuming a frozen turbulence convected in the center of the plane channel. In regard with this figure, the present signal appears smoothed because of the filtering produced by the coarse grids used for performing these PITM simulations. Indeed, the more the grids are coarse, the more the fine grained turbulence is weak and smoothed out, the mesh acting like a low-pass filter reducing the high frequencies. A more detailed analysis of the signal is worked out by computing the energy spectrum densities of one dimensional spectra of the three velocity components. As usually made in signal processing, the one dimensional time spectrum is obtained by taking the windowed fast Fourier transform (FFT) with a Hann window $H(t)$ [56] of the fluctuating velocity correlation tensor as follows

$$E_{ii}(\nu) = FFT[\langle u_i^<(t)u_i^<(t + \tau) \rangle H(t)] \quad (34)$$

for $i = 1, 2, 3$ (no summation). The three spectra E_{11} , E_{22} and E_{33} are presented in figure 18 versus the dimensionless frequency $\nu^* = \nu h/U_b$. To improve the accuracy of the data without any dispersion of the spectrum results, the signals are recorded at 11 different spanwise locations at each temporal iteration δt over which the statistical treatment is performed. The time energy spectra densities shown in figure 18 refer to the center of the flow recirculation zone. As a result, the energy spectrum E_{11} associated with the streamwise velocity component u_1 appears of higher intensity than the other ones E_{22} and E_{33} at very low frequencies. One can observe that the spectra E_{11} , E_{22} and E_{33} present the same regular decay for at least two decades of low frequencies that agree very well with the slope decay $-5/3$ of the Kolmogorov law corresponding to the inertial zone of the spectrum. This outcomes means that the flow in the recirculation zone is

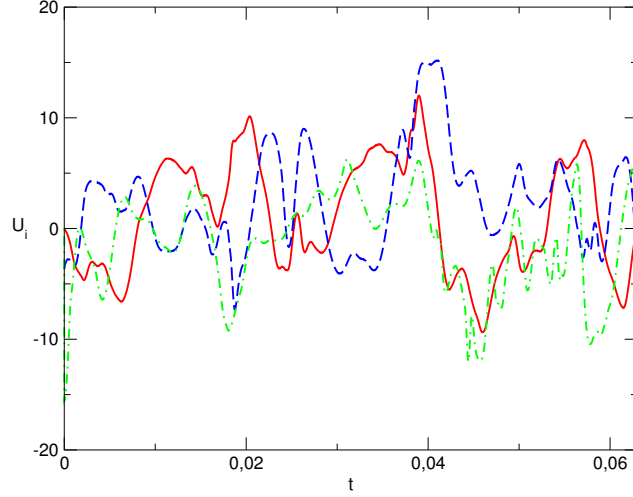


Figure 17: Evolution of the large scale fluctuating velocity $u_i^< = \bar{u}_i - \langle u_i \rangle$ computed in the center of the recirculation zone at $x_1/h = 2$, $x_3/h = 0.5$ versus the time advancement. u_1 : —; u_2 : - - -; u_3 : - . - .; PITM1 simulation ($100 \times 30 \times 100$) performed at $Re = 37000$.

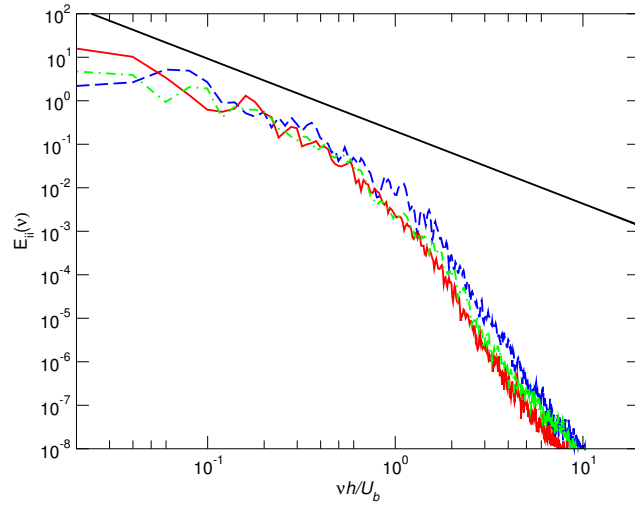


Figure 18: Energy spectrum density of one-dimensional spectra of the three velocity components computed in the center of the recirculation zone at $x_1/h = 2$, $x_3/h = 0.5$. E_{11} : —; E_{22} : - - -; E_{33} : - . - .; $\nu^{-5/3}$: —; PITM1 simulation ($100 \times 30 \times 100$) performed at $Re = 37000$.

close to spectral equilibrium and behaves more or less like locally isotropic turbulence. Afterward, as the frequencies increase, the spectra are characterized by a rapid drop of energy because of the subfilter scale model and of the viscous dissipation process acting in the flow itself. Figure 18 compares very well with figure 17(a) of reference [30] showing the energy spectra density although the spectra are computed at the lower Reynolds number $Re = 10595$. The two set of curves follow similar trends. But the length of the inertial zone should be shorter for the PITM simulations because the physical processes associated with the high frequencies are modeled and consequently not resolved as it is for highly resolved LES.

6.9 Two-point velocity correlation functions

Figure 19 shows an example of the evolutions of two-point correlation functions of the large scale fluctuating of the resolved velocities defined here by

$$R_{ii}(x_1, x_2, x_3) = \frac{\langle u_i^<(x_1, x_2, x_3)u_i^<(x_1, x_2 + r_2, x_3) \rangle}{\sqrt{\langle u_i^<^2(x_1, x_2, x_3) \rangle} \sqrt{\langle u_i^<^2(x_1, x_2 + r_2, x_3) \rangle}} \quad (35)$$

for $i = 1, 2, 3$ (no summation), R_{11} , R_{22} and R_{33} , versus the spanwise distance x_2 where r_2 ranges from 0 to $D_2/2$. The correlation tensor appearing in the numerator is computed using equation

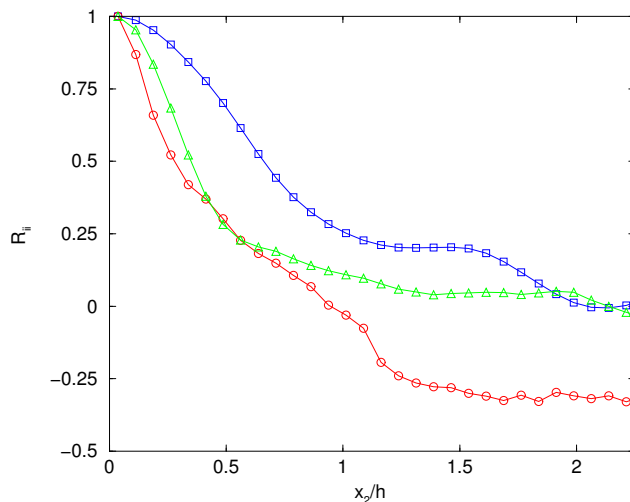


Figure 19: Spanwise two-point correlation function computed at $x_1/h = 6$ and $x_3/h = 1.1$. R_{11} : \circ ; R_{22} : \square ; R_{33} : \triangle ; PITM4 simulation ($160 \times 60 \times 100$) performed at $Re = 37000$.

(10) applied in the case of two different point locations. The correlation is plotted at the streamwise station $x_1/h = 6.0$ at the distance from the wall $x_3/h = 1.1$ allowing a comparison with the curves given on figure 25(d) of reference [30] corresponding to highly resolved LES at the lower Reynolds number $Re = 10595$. Even if the Reynolds number is different, the present calculated evolutions of the two-point correlation functions present qualitative agreements with the data of Fröhlich *et*

al. [30]. But as already observed in reference [30], it appears from figure 19 that the spanwise dimension of the channel is too short because the streamwise tensor correlation R_{11} doesn't return to zero at the mid position of the channel. As the Reynolds number increases from 10590 to 37000, this effect seems more aggravated since R_{11} reaches lower values close to -0.25. Regarding the two-point correlation profiles, the slow decay of the curves associated with R_{22} and R_{33} in that region suggests the presence of elongated eddies in the spanwise direction. This outcome is moreover confirmed by figure 3 showing the longitudinal roll cells in the leeward region of the second hill. Once more, the PITM simulation has provided realistic information on the two-point correlation functions although being performed on coarse meshes.

7 Conclusion

A subfilter stress model derived from the PITM method has been applied to simulate the separated flow in a channel with streamwise periodic constrictions at high Reynolds number. In comparison to highly resolved LES requiring refined meshes, the present simulations have been performed on several meshes including a very coarse mesh, two coarse meshes and a medium mesh. As a result, it has been found that the PITM simulations performed on the meshes $80 \times 60 \times 100$ points (PITM3) $\approx 1/2$ million grid points, and $160 \times 60 \times 100$ (PITM4) ≈ 1 million grid points, respectively in the streamwise, spanwise and normal directions (x_1, x_2, x_3) reproduce fairly well this flow with complex physics involving turbulence mechanisms associated with separation, recirculation, reattachment, acceleration and wall effects. In particular, the mean velocity profiles are in very good agreement with the experimental data although the meshes are coarse, the degree of the mesh refinement used for performing PITM simulations still remaining far away from the one required to perform highly resolved LES. These remarks are particularly true as the Reynolds number increases. In this case, the computational time can be appreciably reduced compared to the one of an highly resolved LES. The main outcome of this study is also to show numerically that the PITM simulations may be damaged if using too coarse mesh resolution, especially in the spanwise direction of the flow. More precisely, it appears that the grid in this direction can indeed be coarse as in the other grid directions in the longitudinal and normal directions, but a sufficient resolution in the spanwise direction is however required to allow the PITM simulation to mimic correctly the turbulent mechanisms induced by three dimensional component. Concerning the other PITM simulations performed on the meshes $80 \times 30 \times 100$ points (PITM1) $\approx 1/4$ million grid points, and $160 \times 30 \times 100$ points (PITM2) $\approx 1/2$ million grid points, the mean velocity and turbulent stresses are found in acceptable agreement with the experimental profiles, some discrepancies being however observed in the immediate vicinity of the lower wall. But we have proven that the origin of this misprediction is essentially due to the spanwise grid resolution and not at all to the model itself. In contrast with the PITM simulations, the statistical RSM computation, whatever the mesh considered, shows important weaknesses in the prediction of this particular flow, mainly because in the statistical approach, no account can be taken of the very large unsteady eddies. This conclusion pertains however only to a particular flow and a particular stress transport closure [25].

A Low Reynolds number formulation of the subfilter scale model

The present subgrid stress PITM model based on the transport equations (12) and (14) has been used in a low Reynolds number form. The modeled expressions of each individual terms of these equations are briefly recalled in the following, the principle of the modeling being developed in references [7, 23]. The production term represents the source due to the interaction between the stresses and the velocity gradients

$$P_{ij} = -(\tau_{ik})_{sfs} \frac{\partial \bar{u}_j}{\partial x_k} - (\tau_{jk})_{sfs} \frac{\partial \bar{u}_i}{\partial x_k} \quad (36)$$

The redistribution term Π_{ij} is decomposed into a slow part Π_{ij}^1 , a rapid part, Π_{ij}^2 and a wall reflection part Π_{ij}^3 . The slow term Π_{ij}^1 (Rotta term) characterizes the return to isotropy due to the action of turbulence on itself

$$\Pi_{ij}^1 = -c_1 \frac{\epsilon_{sfs}}{k_{sfs}} \left((\tau_{ij})_{sfs} - \frac{1}{3} (\tau_{mm})_{sfs} \delta_{ij} \right), \quad (37)$$

the rapid term Π_{ij}^2 (isotropization of production term) involves the velocity gradients

$$\Pi_{ij}^2 = -c_2 \left(P_{ij} - \frac{1}{3} P_{mm} \delta_{ij} \right), \quad (38)$$

and the wall reflexion term Π_{ij}^3 accounts for the wall effects caused by the reflection of the pressure fluctuations from rigid walls

$$\begin{aligned} \Pi_{ij}^3 &= c_{1w} \frac{\epsilon_{sfs}}{k_{sfs}} \left((\tau_{kl})_{sfs} n_k n_l \delta_{ij} - \frac{3}{2} (\tau_{ki})_{sfs} n_k n_j - \frac{3}{2} (\tau_{kj})_{sfs} n_k n_i \right) f_w \\ &+ c_{2w} \left(\Pi_{kl}^2 n_k n_l \delta_{ij} - \frac{3}{2} \Pi_{ik}^2 n_k n_j - \frac{3}{2} \Pi_{jk}^2 n_k n_i \right) f_w \end{aligned} \quad (39)$$

In these expressions, c_1 and c_2 are some functions depending on the Reynolds number and on the anisotropy tensor $(a_{ij})_{sfs} = [(\tau_{ij})_{sfs} - \frac{2}{3} k_{sfs} \delta_{ij}] / k_{sfs}$, the subgrid-scale invariants $A_2 = (a_{ij})_{sfs} (a_{ji})_{sfs}$, $A_3 = (a_{ij})_{sfs} (a_{jk})_{sfs} (a_{ki})_{sfs}$ and the flatness parameter $A = 1 - \frac{9}{8} (A_2 - A_3)$. The quantity n_i is the unit vector perpendicular to the wall and f_w is a near wall damping function. The diffusion terms J_{ij} and J_ϵ appearing in equations (12) and (14), respectively, are modeled assuming a well-known gradient law

$$J_{ij} = \frac{\partial}{\partial x_m} \left(\nu \frac{\partial (\tau_{ij})_{sfs}}{\partial x_m} + c_s \frac{k_{sfs}}{\epsilon_{sfs}} (\tau_{ml})_{sfs} \frac{\partial (\tau_{ij})_{sfs}}{\partial x_l} \right) \quad (40)$$

and

$$J_\epsilon = \frac{\partial}{\partial x_j} \left(\nu \frac{\partial \epsilon_{sfs}}{\partial x_j} + c_\epsilon \frac{k_{sfs}}{\epsilon_{sfs}} (\tau_{jm})_{sfs} \frac{\partial \epsilon_{sfs}}{\partial x_m} \right) \quad (41)$$

where c_s and c_ϵ are constant coefficients. Relatively to its previous value [7], the coefficient c_{ϵ_1} appearing in the subfilter dissipation rate equation (14) is slightly recalibrated to the value $c_{\epsilon_1} =$

Functions	Expressions
R_t	$k_{sfs}^2/(\nu\epsilon_{sfs})$
c_1	$\left([1 + 2.30 A A_2^{1/8} [1 - \exp(-(R_t/140)^2)]\right) \alpha(\eta)$
c_2	$0.60A^{1/2}(1 - \exp(-\sqrt{R_t}))$
c_{1w}	$-\frac{2}{3}c_1 + \frac{5}{3}$
c_{2w}	$\max(\frac{2}{3}c_2 - \frac{1}{6}, 0)/c_2$
f_w	$\min(0.4k_{sfs}^{3/2}/(\epsilon_{sfs}x_n), 2.50)$
α	$(1 + \alpha_1\eta_c^2)/(1 + \alpha_2\eta_c^2)$

Table 2: Functions used in the subfilter stress model.

1.5 instead of $c_{\epsilon_1} = 1.45$. The value $c_{\epsilon_1} = 1.5$ also comes almost naturally in the analytical developments performed in the spectral space [5, 6, 22], although this value is not a theoretical requirement [29]. The functions used in the subgrid-scale model stress at low Reynolds number are listed in table (2). These functions are inspired from the statistical Launder and Shima model [25] when η_c goes to zero (RANS behavior) but are modified to remain consistent with the logarithmic law of the wall in the turbulent boundary layer. Moreover, the constant coefficients appearing in the function c_1 have been optimized to 2.30 and 140 instead of 2.58 and 150 and the dependence with respect to the second invariant is proposed as $A_2^{1/8}$ instead of $A_2^{1/4}$ in order to vary more slowly. According to the rapid distortion theory for homogeneous strained turbulence in an initially isotropic state [57], the function c_2 has been also modified with the aim to satisfy the limiting condition $\lim_{R_t \rightarrow \infty} c_2(R_t) = 0.60$. These new functions are also listed in table (2). The constants values used in the diffusion terms are $c_s = 0.22$ and $c_\epsilon = 0.18$. The numerical coefficients used in the function c_{sfs_1} are $\alpha_1 = 1.3/400$ and $\alpha_2 = 1/400$, $\beta_\eta = [2/(3C_K)]^{9/2}$ is computed for $C_K = 1.4$. In the present calculations, the PITM subfilter model exactly reduces to the corresponding RSM model formulation when used in statistical mode when η_c goes to zero.

References

- [1] Gatski T. B., Rumsey C. L. and Manceau R. Current trends in modelling research for turbulent aerodynamic flows, *Philos. Trans. R. Soc. London, Ser. A* 365, 2389-2418, 2007.
- [2] Schiestel R., *Modeling and simulation of turbulent flows*, (ISTE Ltd and J. Wiley, 2008).
- [3] Hanjalic K. and Launder B. *Modelling turbulence in engineering and the environment*, Cambridge University Press, 2011.
- [4] Chaouat B. Reynolds stress transport modeling for high-lift airfoil flows, *AIAA J.* 44, 2390-2403, 2006.
- [5] Schiestel R. and Dejoan A. Towards a new partially integrated transport model for coarse grid and unsteady turbulent flow simulations, *Theor. Comput. Fluid Dyn.* 18, 443-468, 2005.
- [6] Chaouat B. and Schiestel R. A new partially integrated transport model for subgrid-scale stresses and dissipation rate for turbulent developing flows, *Phys. Fluids* 17, 065106, 1-19, 2005.
- [7] Chaouat B. Subfilter-scale transport model for hybrid RANS/LES simulations applied to a complex bounded flow, *J. Turbul.* 11, 1-30, 2010.
- [8] Lesieur M. and Metais O. New trends in large-eddy simulations of turbulence, *Ann. Rev. J. Fluid Mech.* 28, 45-82, 1996.
- [9] Spalart P. R. Detached-eddy simulation, *Annu. Rev. Fluid Mech.* 41, 181-202, 2009.
- [10] Fröhlich J. and Von Terzi D. Hybrid LES/RANS methods for the simulation of turbulent flows, *Prog. Aerosp. Sci.* 44, 349-377, 2008.
- [11] Shur M. L., Spalart P. R., Strelets M. K. and Travin A. K. A hybrid RANS-LES approach with delayed-DES and wall-modelled LES capabilities, *Int. J. Heat Fluid Flow*, 29, 1638-1649, 2008.
- [12] Spalart P. R., Deck S., Shur M. L., Squires K. D., Strelets M. Kh. and Travin A. A new version of detached-eddy simulation, resistant to ambiguous grid densities, *Theor. Comput. Fluid Dynamics*, 20, 181-195, 2006.
- [13] Egorov Y, Menter F. R. and Cokljat D. Scale-adaptative simulation method for unsteady flow predictions. Part1: Theory and model description, *Flow, Turbul. Combust.*, 85, 113-138, 2010.
- [14] Menter F. R., Kuntz M. and Langtry R. Ten years of industrial experience with the SST turbulence model, *Turb., Heat Mass Transfer*, 4, 2003.
- [15] Menter F. R. Two-Equations Eddy-Viscosity Turbulence Models for Engineering Applications, *AIAA Journal*, 32, 1598-1605, 1994.
- [16] Hamba F. A hybrid RANS/LES simulation of turbulent channel flow, *Theor. Comput. Fluid Dyn.*, 16, 387-403, 2003.
- [17] Tessicini F. and Leschziner M. A. Large eddy simulation of three-dimensional flow around a hill-shaped obstruction with a zonal near-wall approximation, *Int. J. Heat Fluid Flow*, 27, 894-908, 2007.

- [18] Breuer M., Jaffrézic B. and Arora K. Hybrid LES-RANS techniques based on a one-equation near-wall model, *Theor. Comput. Fluid Dyn.*, 22, 157-187, 2009.
- [19] Davidson L. and Billson M. Hybrid LES-RANS using synthesized turbulent fluctuations for forcing in the interface region, *Int. J. Heat Fluid Flow*, 27, 1028-1042, 2006.
- [20] Hamba F. Log-layer mismatch and commutation error in hybrid RANS/LES simulation of channel flow, *Int. J. Heat Fluid Flow*, 30, 20-31, 2009.
- [21] Chaouat B. Simulation of turbulent rotating flows using a subfilter scale stress model derived from the partially integrated transport modeling method, *Phys Fluids*, 24, 045108, 1-35, 2012.
- [22] Chaouat B. and Schiestel R. From single-scale turbulence models to multiple-scale and subgrid-scale models by Fourier transform, *Theor. Comput. Fluid Dyn.* 21, 201-229, 2007.
- [23] Chaouat B. and Schiestel R. Progress in subgrid-scale transport modelling for continuous hybrid non-zonal RANS/LES simulations, *Int. J. Heat Fluid Flow*, 30, 602-616, 2009.
- [24] Fadai-Ghotbi A., Friess C., Manceau R., Gatski T. B. and Borée J. Temporal filtering: A consistent formalism for seamless hybrid RANS-LES modeling in inhomogeneous turbulence, *Int. J. Heat Fluid Flow*, 31, 378-389, 2010.
- [25] Launder B. E. and Shima N. Second Moment Closure for the Near Wall Sublayer: Development and Application, *AIAA Journal*, 27, 1319-1325, 1989.
- [26] Speziale C. G., Sarkar S. and Gatski T. B. Modelling the Pressure-Strain Correlation of Turbulence: an Invariant Dynamical Systems Approach, *Journal of Fluid Mechanics*, 227, 245-272, 1991.
- [27] Chaouat B. An efficient numerical method for RANS/LES turbulent simulations using subfilter scale stress transport equations, *Int. J. Numer. Meth. Fluids*, 67, 1207-1233, 2011.
- [28] Girimaji S. S., Jeong E. and Srinivasan R. Partially averaged Navier-Stokes method for turbulence: Fixed point analysis and comparisons with unsteady partially averaged Navier-Stokes, *ASME J. Appl. Mech.*, 73, 3, 422-429, 2006.
- [29] B. Chaouat and R. Schiestel, Analytical insights into the partially integrated transport modeling method for hybrid Reynolds averaged Navier-Stokes equations-large eddy simulations of turbulent flows, *Phys. Fluids*, 24, 085106, 1-34, 2012.
- [30] Fröhlich J., Mellen C., Rodi W., Temmerman L. and Leschziner M. Highly resolved large-eddy simulation of separated flow in a channel with streamwise periodic constriction, *J. Fluid Mech.*, 526, 19-66, 2005.
- [31] Breuer M., Peller N., Rapp C. and Manhart M. Flow over periodic hills. Numerical and experimental study in a wide range of Reynolds numbers, *Comput. Fluids* 38, 433-457, 2009.
- [32] Rapp C. Experimentelle Studie der turbulenten Strömung über periodisches Hügel, Ph.D thesis, Technische Universität München, Germany, 2009.
- [33] Rapp C. and Manhart M. Flow over periodic hills - an experimental study, *Exp. Fluids*, 51, 247-269, 2011.

- [34] Lumley J. L. Computational Modeling of Turbulent Flows, *Advances Applied Mech.*, 18, 123-176, 1978.
- [35] Schiestel R. Sur le concept d'échelles multiples en modélisation des écoulements turbulents. Part I, *J. Theor. Appl. Mech.* 2, 417-449, 1983.
- [36] Schiestel R. Sur le concept d'échelles multiples en modélisation des écoulements turbulents. Part II, *J. Theor. Appl. Mech.* 2, 601-628, 1983.
- [37] Chaouat B. and Schiestel R. On partially integrated transport models for subgrid-scale modelling, *ERCOFTAC Bulletin* 72, 49-54, 2007.
- [38] Befeno I. and Schiestel R. Non-equilibrium mixing of turbulence scales using a continuous hybrid RANS/LES approach: Application to the shearless mixing layer Flow, *Turbul. Combust.* 78, 129-151, 2007.
- [39] Jakirlic S., Manceau R., Saric S., Fadai-Ghotbi A., Kniesner B., Carpy S., Kadavelil G., Friess C., Tropea C. and Borée J. LES, zonal and seamless hybrid LES/RANS: Rationale and applications to free and wall-bounded flows involving separations and swirl, *Numerical simulation of turbulent flows and noise generation*, Ed. Brun C, Juve D, Manhart M and Munz C. D. by Springer, 104, 253-282, 2009.
- [40] Chaouat B. and Schiestel R. Continuous hybrid non-zonal RANS/LES simulations of flows over periodic hills at different Reynolds numbers using the PITM method, *10nd Engineering Turbulence Modelling and Measurements*, 2, 552-557, 2010.
- [41] Chaouat B. Numerical predictions of channel flows with fluid injection using Reynolds stress model, *J. Propul. Power* 18, 295-303, 2002.
- [42] Speziale C. G, Abid R. and Durbin P. A. On the Realisability of Reynolds Stress Turbulence Closures, *J. Scient. Comput.*, 9, 369-403, 1994.
- [43] Fadai-Ghotbi A., Friess C., Manceau R. and Borée J. A seamless hybrid RANS-LES model based on transport equations for the subgrid stresses and ellipting blending, *Phys. Fluids* 22, 055104, 1-19, 2010.
- [44] Germano M., Piomelli U., Moin P. and Cabot W. H. A dynamic subgrid-scale eddy-viscosity model, *Phys. Fluids* 3, 1760-1765, 1992.
- [45] Manceau R., Bonnet J. P, Leschziner M. A. and Menter F. 10th joint ERCOFTAC (SIG-15)/IAHR/QNET-CFD Workshop on refined flow modelling, Poitiers, Ed. by Manceau R, Bonnet J. P, Leschziner M. A. and Menter F. LEA, CNRS/Université de Poitiers, France, october, 2002.
- [46] Nicoud F. and Ducros F. Subgrid-scale modelling based on the square of the velocity gradient tensor, *Flow, Turbul. Combust.*, 62, 183-200, 1999.
- [47] Jakirlic S., Saric S., Kadavelil G., Sirbubalo E., Basara B. and Chaouat B. SGS modelling in LES of wall-bounded flows using transport RANS models: from a zonal to a seamless hybrid LES/RANS method, *Proceeding of the 6nd Symposium on Turbulent Shear Flow Phenomena* edited by Kasagi N, Eaton J, Friedrich R, Humphrey J, Johansson A. and Sung H. 3, 1057-1062, 2009.

- [48] Manhart M., Rapp C., Peller N., Breuer M., Aybay O., Denev J. and Falconi J. Assessment of eddy resolving techniques for the flow over periodically arranged hills up to $Re=37,000$, Quality and Reliability of Large Eddy Simulations II, Ed. Springer Verlag by Salvetti M. V., Geurts B., Meyers J. and Sagaut J. P., 16, 361-370, 2011.
- [49] Smagorinsky J. General circulation experiments with the primitive equations, *Mon. Weather Rev.* 91, 99-164, 1963.
- [50] Meneveau C., Lund T. S. and Cabot W. H. A Lagrangian dynamic subgrid-scale model of turbulence, *J. Fluid Mech.*, 319, 353-385, 1996.
- [51] Denev J., Falconi C., Fröhlich J. and Bockhorn H. Wavelet-adaptated subgrid-scale models for LES, Second Int. Conf. on Turbulence and Interaction, june, 2009.
- [52] Schumann U. Subgrid Scale Model for Finite Difference Simulation of Turbulent Flows in a Plane Channel Annuli, *J. Comput. Phys.*, 18, 367-404, 1975.
- [53] Piomelli U. and Chasnov J. R. Large eddy simulations: theory and applications, *Turbulence and Transition Modelling*, Edited by Hallback M, Henningson D, Johansson A and Alfredson P, Kluwer, 269-331, 1996.
- [54] Dubief Y. and Delcayre F. On coherent-vortex identification in turbulence, *J. Turbul.*, 1, 1-22, 2000.
- [55] Schumann U. Realizability of Reynolds Stress Turbulence Models, *Phys. Fluids*, 20, 721-725, 1977.
- [56] Press W. H., Teukolsky S. A, Vetterling W. T. and Flannery B. P. *Numerical recipes*, Cambridge University Press, 1992.
- [57] Crow S. C. Viscoelastic properties of the fine-grained incompressible turbulence, *J. Fluid Mech.* 33, 1-20, 1968.